Slow particle remineralization, rather than suppressed disaggregation, drives efficient flux transfer through the Eastern Tropical North Pacific Oxygen Deficient Zone

24 May 2021

Jacob A. Cram[1,] Clara A. Fuchsman[1], Megan E. Duffy[2], Jessica L. Pretty[3], Rachel M. Lekanoff[3],
Jacquelyn A Neibauer[2], Shirley W. Leung[2], Klaus B. Huebert[1], Thomas S. Weber[4], Daniele Bianchi[5],
Natalya Evans[6], Allan H. Devol[2], Richard G. Keil[2], Andrew M.P. McDonnell[3]

[1]Horn Point Laboratory, University of Maryland Center for Environmental Science, Cambridge, MD, USA.

[2]School of Oceanography, University of Washington Seattle, Seattle, WA, USA.

[3]College of Fisheries and Ocean Sciences, University of Alaska Fairbanks, Fairbanks, AK, USA.

[4]School of Arts and Sciences, University of Rochester, Rochester, NY, USA.

[5]Department of Atmospheric and Oceanic Sciences, University of California Los Angeles, Los Angeles, CA, USA.

[6]Department of Biological Sciences, University of Southern California, Los Angeles, CA, USA.

1 Key Points

The upper mesopelagic of the oligotrophic Eastern Tropical North Pacific Oxygen Deficient Zone (ODZ) has low flux attenuation.

Comparison of particle size observations to models suggests that the breakdown of particles of all sizes is slow throughout the ODZ.

Zooplankton appear to transport organic matter into, and disaggregate particles within, the ODZ above 500 m.

1

2 Abstract

Models and observations suggest that particle flux attenuation is lower across the mesopelagic zone of anoxic environments compared to oxic ones. Flux attenuation is controlled by microbial metabolism as well as aggregation and disaggregation by zooplankton, all of which also shape the relative abundance of different sized particles. Observing and modeling particle spectra can provide information about the contributions of these processes. We measured particle size spectrum profiles at one station in the oligotrophic Eastern Tropical North Pacific Oxygen Deficient Zone (ETNP ODZ) using an underwater vision profiler (UVP), a high-resolution camera that counts and sizes particles. Measurements were taken at different times of day, over the course of a week. Comparing these data to particle flux measurements from sediment traps collected over the same time-period allowed us to constrain the particle size to flux relationship, and to generate highly resolved depth and time estimates of particle flux rates. We found that particle flux attenuated very little throughout the anoxic water column, and at some time-points appeared to increase. Comparing our observations to model predictions suggested that particles of all sizes remineralize more slowly in the ODZ than in oxic waters, and that large particles disaggregate into smaller particles, primarily between the base of the photic zone and 500 m. Acoustic measurements of multiple size classes of organisms suggested that many organisms migrated, during the day, to the region with high particle disaggregation. Our data suggest that diel-migrating organisms both actively transport biomass and disaggregate particles in the ODZ core.

3 Plain Language Summary

Marine snow are microscopic particles that form in the surface of the ocean and sink into the deep ocean. Most of these particles are the remains of dead algae and feces of tiny animals (zooplankton). The deeper the particles sink into the ocean before microbes or animals consume them, the longer it takes before the carbon in those particles can return to the atmosphere. In parts of the ocean where there is no oxygen, more particles sink to greater depths, for reasons that are not well-understood. We used an underwater camera to observe marine snow particles in the ocean just west of Mexico where there is little to no oxygen at depth. We compared the observations to predictions from several computer simulations representing hypothesized mechanisms to explain why particles are consumed less in water without oxygen. Our measurements suggest that one reason that particles sink to deeper depths here is because microbes consume the particles slowly when there is no oxygen. Meanwhile, zooplankton still break large particles into smaller ones and produce fecal pellets in these low oxygen waters.

4 Introduction

The biological pump, in which sinking particles transport carbon from the surface into the deep ocean, is a key part of the global carbon cycle (Neuer et al., 2014; Turner, 2015). Organic matter flux into the deep ocean is a function both of export from the photic zone into the mesopelagic (export flux), and the fraction of that flux that crosses through the mesopelagic (transfer efficiency) (Francois et al., 2002; Passow & Carlson, 2012; Siegel et al., 2016). The transfer efficiency of the biological pump may affect global atmospheric carbon levels (Kwon & Primeau, 2008). Thus, understanding the processes that shape organic matter degradation in the mesopelagic is critical.

Zooplankton modulate carbon flux through the mesopelagic (Jackson & Burd, 2001; Steinberg & Landry, 2017; Turner, 2015), and by extension the efficiency of the biological pump (Archibald et al., 2019; Cavan et al., 2017). They affect particle flux through four processes: *repackaging*, *respiration*, *active transport* and *disaggregation*. Zooplankton *repackage* particles into fecal pellets that have different properties from the original particles they ingest (Wilson et al., 2008). The repackaged particles may be egested at greater depth in the water column during the zooplankton's migration, resulting in the *active transport* of organic carbon over depth (Archibald et al., 2019; Bianchi et al., 2013; Hannides et al., 2009; Steinberg et al., 2000; Stukel et al., 2018, 2019). In addition to repackaging, zooplankton may *respire* some proportion of the particles' organic matter by consuming particles in the mesopelagic (Stukel et al., 2019). Suspension feeding zooplankton did not substantially attenuate flux in the California Current system (Stukel et al., 2019). Zooplankton break large particles into smaller ones, likely by generating turbulence when they swim (Dilling & Alldredge, 2000; Goldthwait et al., 2005). This *disaggregation* can lead to increased remineralization of particles because those smaller particle pieces sink more slowly and so have longer residence times in the mesopelagic, causing them to be consumed before reaching deep waters (Goldthwait et al., 2005). This fragmentation has been shown in some cases to explain around 50% of flux attenuation (Briggs et al., 2020).

Oxygen concentrations, and the geographic and depth range of anoxic ocean regions, appear to modulate particle flux through the mesopelagic. Observations of particle flux in the Eastern Tropical North Pacific near the Mexican coast (Hartnett & Devol, 2003; Van Mooy et al., 2002; Weber & Bianchi, 2020), the Eastern Tropical South Pacific (Pavia et al., 2019), and Arabian Sea (Keil et al., 2016; Roullier et al., 2014) have suggested lower flux attenuation in these ODZ systems. Models have shown that accounting for oxygen limitation in ODZs is necessary to fit global patterns of particle transfer (Cram et al., 2018; DeVries & Weber, 2017). Analysis of remineralization tracers also shows evidence of slow flux attention in the ODZs (Weber & Bianchi, 2020). The oxygen content of the ocean is decreasing (Ito et al., 2017; Schmidtko et al., 2017), and the spatial extent and depth range of ODZs, including the ETNP ODZ are

3

87 likely to change, though there is disagreement over whether they are expanding or undergoing natural
88 fluctuation (Deutsch et al., 2014; Horak et al., 2016; Stramma et al., 2008). Changes to ODZ ranges are
89 likely to affect ocean chemistry, the habitat of marine organisms, and the interactions between organisms
90 and chemistry (Gilly et al., 2013). Models and chemical data suggest that ODZs may enhance carbon
91 transport to the deep ocean, by inhibiting microbial degradation of sinking marine particles (Cram et al.,
92 2018). However, biological organic matter transport is also modulated by zooplankton whose interactions
93 with particle flux in pelagic ODZs are only beginning to be explored (Kiko et al., 2020).

94 Models of particle transfer through the mesopelagic oceans predict that particle size, ocean temperature,
95 and oxygen concentrations are the dominant factors modulating particle flux attenuation (Cram et al.,
96 2018; DeVries & Weber, 2017). These models, however, do not account for active transport or
97 disaggregation by zooplankton. As a result of this assumption, the models predict that small particles
98 preferentially attenuate with depth, which is often not borne out by observations (Durkin et al., 2015).
99 Therefore, these models' predictions provide a useful null hypothesis of expected particle size
100 distributions in the absence of zooplankton effects, which can be compared to observed distributions of
101 particles to explore the magnitude of zooplankton effects.

102 Underwater vision profilers are cameras that can count and size many particles over large water volumes
103 (Picheral et al., 2010) and provide valuable information about particle distributions and transport. When
104 deployed in concert with particle traps in some regions, they can be used to predict flux in other regions
105 where traps have not been deployed (Guidi et al., 2008; Kiko et al., 2020). UVPs can provide information
106 about. Connecting UVP and trap data can furthermore inform about total particle flux variability across
107 space and time, relationships between particle size, biomass, composition, and sinking speed, as well as
108 the contributions of the different particle sizes to flux (Guidi et al., 2008; Kiko et al., 2017).

109 UVP have provided insight into other anoxic and hypoxic environments. In the Arabian Sea, particle size
110 data from a UVP were compared to measurements zooplankton abundances and surface productivity. The
111 authors concluded that in this ODZ region, particle size distributions were shaped by microbial and
112 zooplankton activity, the spatiotemporal structure of surface phytoplantkon blooms, and horizontal
113 transport of particles by currents (Roullier et al., 2014). Another recent study combined new particle size
114 tracking, mockness tows, and acoustic data, all collected at one site, with previously collected trap
115 measurements from nearby locations to explore zooplankton transport in the Eastern Tropical North
116 Atlantic, a hypoxic, but not anoxic, Oxygen Minimum Zone (OMZ) (Kiko et al., 2020). The authors
117 found a particle concentration maximum in the mesopelagic and contend that this feature suggests
118 transport by zooplankton, and/or mortality of migrating zooplankton. The authors suggest that in more
119 anoxic and larger ODZs, such as the modern day ETNP, and in particular as hypoxic water shifts to

4

120   anoxia, there might be reduced active transport into the mesopelagic, since many migratory organisms

121   would presumably not migrate into the anoxic water and would be less active. In this manuscript we

122   provide data from such a fully anoxic region.

123   A recent modeling study posed three hypotheses to explain why particle flux attenuates slowly in ODZs

124   (Weber & Bianchi, 2020), which are susceptible to testing with UVP data. These are: **H1:** *All* particles in

125   ODZs remineralize more slowly than in oxic water, regardless of their size, due to slower carbon

126   oxidation during denitrification than aerobic respiration. **H2:** Disaggregation by zooplankton is slower in

127   ODZs than elsewhere. **H3:** Large particles remineralize more slowly in ODZs, but smaller ones do not,

128   because carbon oxidation in large particles can become limited by the diffusive supply of oxygen and

129   nitrate. In this case, respiration can only proceed by thermodynamically inefficient sulfate reduction

130   (Bianchi et al., 2018; Lam & Kuypers, 2011). Sulfide and organic matter sulfurization have been found on

131   particles at this site at nanomolar concentrations (Raven et al., 2021). Microbial analysis of particles

132   found sulfate reducers and S-oxidizing denitrifiers at low abundance (Fuchsman et al., 2017; Saunders et

133   al., 2019). Each of the hypotheses outlined above were predicted to leave distinct signatures in particle

134   size distributions in the core of ODZ regions (Weber & Bianchi, 2020). The model with slow attenuation

135   of all particles, predicts an increase in the abundance of small particles in the ODZ core (**H1**), while the

136   other two models predict a decrease in small particle abundance, because small particles are either not

137   replaced by disaggregation of large particles (**H2**) or because those particles are remineralized more

138   quickly than larger particles (**H3**). However, the necessary particle size data from an ODZ was not

139   available to support any hypothesis at the exclusion of the others. In this manuscript we present a new

140   dataset that is sufficient to test these three hypotheses.

141   While UVP and traps have been sampled together (Guidi et al., 2008), combined trap and UVP

142   measurements have not been taken together previously in an ODZ. Most of the volume of the ETNP ODZ

143   is below regions of very low surface productivity (Fuchsman et al., 2019; Pennington et al., 2006).

144   Meanwhile most flux data have been measured in more coastal, higher productivity regions of the ETNP

145   (Hartnett & Devol, 2003; Van Mooy et al., 2002). Furthermore, the degree to which zooplankton

146   swimming or other processes lead to particle disaggregation, both in ODZs and elsewhere in the ocean, is

147   unknown.

148   To provide the data to test hypotheses **H1-H3** and illuminate zooplankton particle interactions in

149   oligotrophic ODZs, we collected particle size data at high temporal resolution over the course of a week

150   in an anoxic site typical of the oligotrophic ETNP ODZ, well away from the high productivity zone in the

151   coast. We integrated this size data with observed flux measurements, and acoustic data. We quantified,

5

152	throughout the water column, how changes in size distribution deviate from changes that would be
153	predicted by remineralization and sinking only models.

154	We ask the following three questions:

155	**Question A:** Do our data support any of the three Weber and Bianchi (2020) models (**H1-H3**)?

156	**Question B:** How does the particle size distribution at one location in the oligotrophic Eastern Tropical
157	North Pacific vary with respect to depth and time?

158	**Question C:** Do our data suggest that regions of the oxygen deficient zone harbor disaggregation like
159	processes, and if so, do these co-occur with migratory zooplankton?

5 *Methods*

161	Unless specified otherwise, measurements were taken on board the R/V *Sikuliaq*, cruise number
162	SKQ201617S, from 07 January 2017 through 13 January 2017 at a single station 16.5°N 106.9°W, which
163	was located in an oligotrophic region of the Eastern Tropical North Pacific Oxygen Deficient Zone
164	(ETNP Station P2; Figure 1A). Data are compared against measurements taken at 16.5°N 152.0°W on 08
165	May 2015, collected on the GO-SHIP CLIVAR/CARBON P16N Leg 1 Cruise (CCHDO Hydrographic
166	Cruise 33RO20150410). This station was at the same latitude as ETNP Station P2, west of the ODZ, but
167	was not anoxic (P16 Transect Station 100; Figure S1).

5.1 Water property measurements

169	We measured water properties of temperature, salinity, fluorescence, oxygen concentration and turbidity
170	using the shipboard SeaBird 911 CTD. Auxiliary sensors included a WetLabs C-Star (beam attenuation
171	and transmission) and a Seapoint fluorometer. Data were processed with Seabird Software, (programs–
172	data conversion, align, thermal mass, derive, bin average and bottle summary) using factory supplied
173	calibrations. Data was analyzed and visualized in *R* (Team 2011). Processed data are available under
174	NCEI Accession number 1064968 (Rocap et al., 2017).

5.2 Water mass analysis

176	Evans et al. (2020) previously employed optimum multiparameter analysis to map the percent identity of
177	the water observed at each depth to three water masses: the 13 Degree Celsius Water (13CW), North
178	Equatorial Pacific Intermediate Water (NEPIW), and Antarctic Intermediate Water (AAIW). We subset
179	and examine only the portion of these data that correspond to our site.

6

5.3 Particle size measurements

Particle size data were collected by Underwater Vision Profiler 5 (UVP) that was mounted below the CTD-rosette and deployed for all CTD casts shallower than 2500 m. A UVP is a combination camera and light source that quantifies the abundance and size of particles from 100 μm to several centimeters in size (Picheral et al., 2010). Visual inspection of images larger than 1 mm suggests that particles are primarily "marine snow" but about 5% are zooplankton. UVP data were processed using custom MATLAB scripts, uploaded to EcoTaxa (Picheral et al., 2017), and analyzed in R. The UVP provided estimates of particle abundances of particles in different size-bins, as well as information about the volumes over which those particle numbers had been collected.

5.4 Flux measurements

Free floating, surface tethered particle traps were used to quantify carbon fluxes from sinking particles. Arrays, consisting of a surface float and two traps, were deployed and allowed to float freely for at least 21-96 hours, during which time they collected and incubated particles. Trap deployments began on 07 January, concurrently with the beginning of the UVP sampling, and continued through 12 January. Trap recovery began on 08 January and continued through 13 January. Trap depths spanned the photic zone and mesopelagic, with the shallowest at 60 m and the deepest at 965 m. Trap deployments lasted between 21 and 93 hours, with deeper traps left out for longer, to collect more biomass. Two types of traps were deployed. One set of traps, generally deployed in shallower water, had a solid cone opening with area 0.46 m^2. The second set had larger conical net with opening of 1.24 m^2 area made of 53 μm nylon mesh similar to the description in Peterson et al. (2005). In all cases, particles collected in the net or cone fell into one of two chambers. The bottom chamber collected particles from the net and incubated them -- we did not use these samples in this study. The top chamber collected particles for 22-27 hours. When the door at the top of the trap closed, the trap was returned immediately to the surface. For some traps, in order to increase collection time, the door between the bottom and top chamber was never closed, in which case we sampled from the combined volume. This meant that these traps had a longer effective collection time of 33-35 hours (69m, 365m 452 m). The trap at 965 m was deployed for an extended period such that collection time was effectively 91 hours. No poisons were used, and living zooplankton, or 'swimmers', were manually removed from collection bottles, while zooplankton carcasses were retained.

Sediment trap material was filtered immediately upon trap recovery onto pre-combusted GF-75 45mm filters (nominal pore size of 0.3 μm) and preserved until further analysis at -80°C. These filters were split into several fractions for other analyses not discussed here. Total carbon content of particles in each trap were measured by isotope ratio mass spectrometry. Elemental analyses for particulate carbon and nitrogen

7

213   quantities as well as ^{13}C and ^{15}N isotopic compositions were conducted at the U.C. Davis Stable Isotope

214   Facility (http://stableisotopefacility.ucdavis.edu) on acidified freeze-dried trap samples to capture organic

215   elemental contributions. Mass spectrometry failed to detect carbon above detection limits in four surface

216   traps, which were excluded from the analysis. Traps at similar depths did detect carbon, lending

217   confidence to the idea that these non-detections were technical in nature, rather than reflecting

218   environmental conditions.

5.5   Analysis

220   All analyses focused on the mesopelagic, defined here as the region between the base of the secondary

221   chlorophyll maximum layer (160 m) (hereafter photic zone), which is below the upper oxycline, and 1000

222   m. For many analyses, including visualizations that include the photic region, particles were binned by

223   depth with 20 m resolution between the surface and 100 m, 25 m resolution between 100m and 200 m

224   depths and 50m resolution below 200 m. This increasing coarseness of the depth bins helped account for

225   more scarce particles deeper in the water column, while maintaining higher depth resolution near the

226   surface. To perform this binning, particle numbers, and volumes of water sampled of all observations

227   within each depth bin were summed prior to other analyses.

228   Two normalized values of particle numbers were calculated. In the first, particle numbers were divided by

229   volume sampled, to generate values in *particles/m³*. In the second, particles were divided by both volume

230   sampled and the width of the particle size-bins to generate values in *particles/m³/mm*.

5.5.1   Particle size distribution

232   We determined the slope and intercept of the particle size distribution spectrum by fitting a power law to

233   the data, which is a common function for fitting particle size distributions (Buonassissi & Dierssen,

234   2010). Because large particles were infrequently detected, we used a general linear model that assumed

235   residuals of the data followed a negative-binomial (rather than normal) distribution. We fit the equation

236     $\ln\left(\frac{E(Total\ Particles)}{Volume * Binsize}\right) = b_0 + b_1\ ln(Size)$ (Eqn 1).

237   to solve for the Intercept (b_0) and particle size distribution slope (PSD = b_1). On the left-hand side of Eqn

238   1. *E(Total Particles)* refers to the expected number of particles in a given depth and particle size bin

239   assuming a negative binomial distribution of residuals (Date, 2020; Ooi, 2013). *Volume* indicates the

240   volume of water sampled by the UVP, or in the case of depth-binned data, the sum of the volumes of all

241   UVP images in that depth interval. *Binsize* indicates the width of the particle-size bin captured by the

242   UVP. Thus, if particles between .1 and 0.12 mm are in a particle size bin, the *Binsize* is 0.02. On the right

243   hand side of Eqn 1., *Size* corresponds to the lower bound of the particle size-bin. We use the lower bound

244   of a particle size-bin, rather than its midpoint, because, due to the power-law particle size distribution

8

245 slopes, the average size of particles in each size-bin is closer to the size-bin's lower bound rather than its
246 midpoint.

5.5.2 Estimating particle flux

248 We estimated particle flux throughout the water column, by fitting particle data to trap measurements. We
249 assumed that particle flux in each size bin (j) followed the equation

250 $$\text{Flux} = \sum_j \left[\frac{Total\ Particles_j}{Volume * Binsize_i} * C_f * (Size_j)^A \right] \quad \text{(Eqn. 2)}$$

251 Such that flux at a given depth is the sum of all size-bin specific values.

252 We used the *optimize()* function in *R*'s stats package to find the values of C_f and A that yielded closest
253 fits of the UVP estimated flux to each particle trap.

254 We also estimated the exponent of the particle size to biomass exponent α and size to sinking speed
255 exponent γ per the equations $\text{Biomass}_j \sim \text{Size}_j^\alpha$ and $\text{Speed}_j \sim \text{Size}_j^\gamma$. This is done by assuming a
256 spherical drag profile, in which case $A = \alpha + \gamma$ and $\gamma = \alpha - 1$ (Guidi et al., 2008).

5.5.3 Size specific information

258 We separately analyzed total particle numbers, particle size distribution, and particle flux for particles
259 larger than or equal to 500 μm, and those smaller than 500 μm, to determine the relative contributions of
260 these two particle classes to particle properties. 500 μm was chosen as it has been previously defined as
261 the cutoff point between microscopic "microaggregates" and macroscopic "marine snow" (Simon et al.,
262 2002).

5.6 Variability

264 To explore the timescales of temporal variability in the POC flux, we determined how well the flux at
265 each depth horizon can be described by the sum of daily and hourly temporal modes. This was achieved
266 by fitting the general additive model of form

267 $\text{Flux}^{1/5} \sim s(\text{Depth}) + s(\text{Day}) + s(\text{Hour})$ (Eqn. 3)

268 This model explored whether estimated flux levels appeared to vary by decimal day and decimal hour,
269 holding the effects of depth constant, in the 250 m to 500 m region. The smooth terms *s* for *Depth* and
270 *Day* were thin plate splines, while the *s* term for *Hour* was a cyclic spline of 24-hour period.

9

5.7 Smoothing for Comparison to Model Results

Normalized particle abundance data, from the only UVP cast that traversed the top 2000m of the water column, taken on January 13 at 06:13, was smoothed with respect to depth, time, and particle size using a general additive model of form

$$\ln \left(\frac{E(Total\ Particles)}{Volume * Binsize} \right) \sim s\big(\text{Depth, } \ln(\text{Size})\big) \qquad \text{(Eqn. 4)}$$

In this case, there is a single, two-dimensional, smooth term, rather than additive one-dimensional terms as in Eqn. 3 so that the smooth term can consider interactions between the two parameters, rather than assuming that the terms are additive. The predicted particle numbers at each particle size and depth, as well as particle size distribution spectra, and estimated particle masses of all particles smaller than 500 μm and all particles larger than or equal to 500 μm were then compared to each of Weber and Bianchi's (2020) models, corresponding to our **H1-H3**.

5.8 Modeling remineralization and sinking

To quantify disaggregation, our goal was to compare the particle size-abundance spectrum at each depth to a prediction of the null hypothesis, that it is simply governed by the effects of sinking and remineralization reshaping the spectrum observed shallower in the water column. This prediction is generated using the particle remineralization and sinking model (PRiSM), modified from DeVries et al. (2014), which we applied to the shallower spectrum as an initial condition. The difference between the null hypotheses prediction and observation indicates of the role of processes not accounted for in PRiSM, such as disaggregation, aggregation, and active or advective transport of particles with a different size spectrum than the ones seen at the deeper depth.

In practice we expanded the previous numerical implementation of PRiSM to allow for particle size distribution spectra with particle-size bins that match those obtained by the UVP, and to return estimates of the number of particles in those same size bins (Text S1). The model accepts inputs of particle size distributions at each depth, and changes in particle flux between each depth and the depth-bin one depth deeper in the water column. The model optimizes a particle remineralization rate that would result in that observed flux loss. It finally returns a "predicted" particle size distribution spectrum that has total flux equal to the flux of the observed deeper spectrum that would be expected if the shallower spectrum only sank and remineralized. In cases where flux increased with depth, particles are assumed to put on mass rather than lose mass following a negative remineralization rate. While there is no biological basis for "negative remineralization", flux increases in the model tend to be close to zero, and this negative remineralization allows our null model to be robust to flux increases when they occur.

10

6 Results

6.1 Physical and Chemical Data

The ODZ, characterized in this study by oxygen levels less than 1 μM, as measured by the CTD, extends from 90 m to 900 m depth, with a sharp upper oxycline and a gradual lower oxycline (Figure 1B-C). This station has been previously proven to be anoxic with a STOX sensor (Tiano et al., 2014). The upper oxycline tracks a sharp pycnocline (Figure 1B-1D), set by the high salinity of the 13CW water mass (Figure S2), and is characterized by an abrupt drop in temperature below the mixed layer and an increase in salinity (Figure 1B). Water mass analysis indicated that water in the top part of the ODZ is dominated by the 13CW water mass, while water between 275 and 500m is primarily from the NEPIW, with water from the AAIW dominating in the lower 500 m (Figure S2) (Evans et al., 2020). The site is characterized by two fluorescence maxima (Figure 1C). The larger, shallower fluorescence peak is positioned just above the oxycline, with fluorescence from this peak and oxygen attenuating together. The smaller, lower peak is inside of the ODZ. For the purposes of this study, we define the photic zone as ending at the base of this deeper fluorescence layer (160m). This photic zone base corresponds with photosynthetically active radiation (PAR) $< 10^{-5}$ of surface PAR levels (Figure 1C). We note that this photic zone depth is deeper than conventional definitions, in which the base of the photic zone corresponds with 10^{-2} (90 m) or 10^{-3} (120 m) of surface PAR. Turbidity tracks the two chlorophyll peaks in the surface and has a tertiary maximum at the lower oxycline (Figure 1D). The cyanobacteria at the secondary chlorophyll maximum are known to be photosynthesizing and producing organic matter in the ODZ (Fuchsman et al., 2019; Garcia-Robledo et al., 2017). To avoid complication due to this source of organic matter production, we focus our further analysis below 160m.
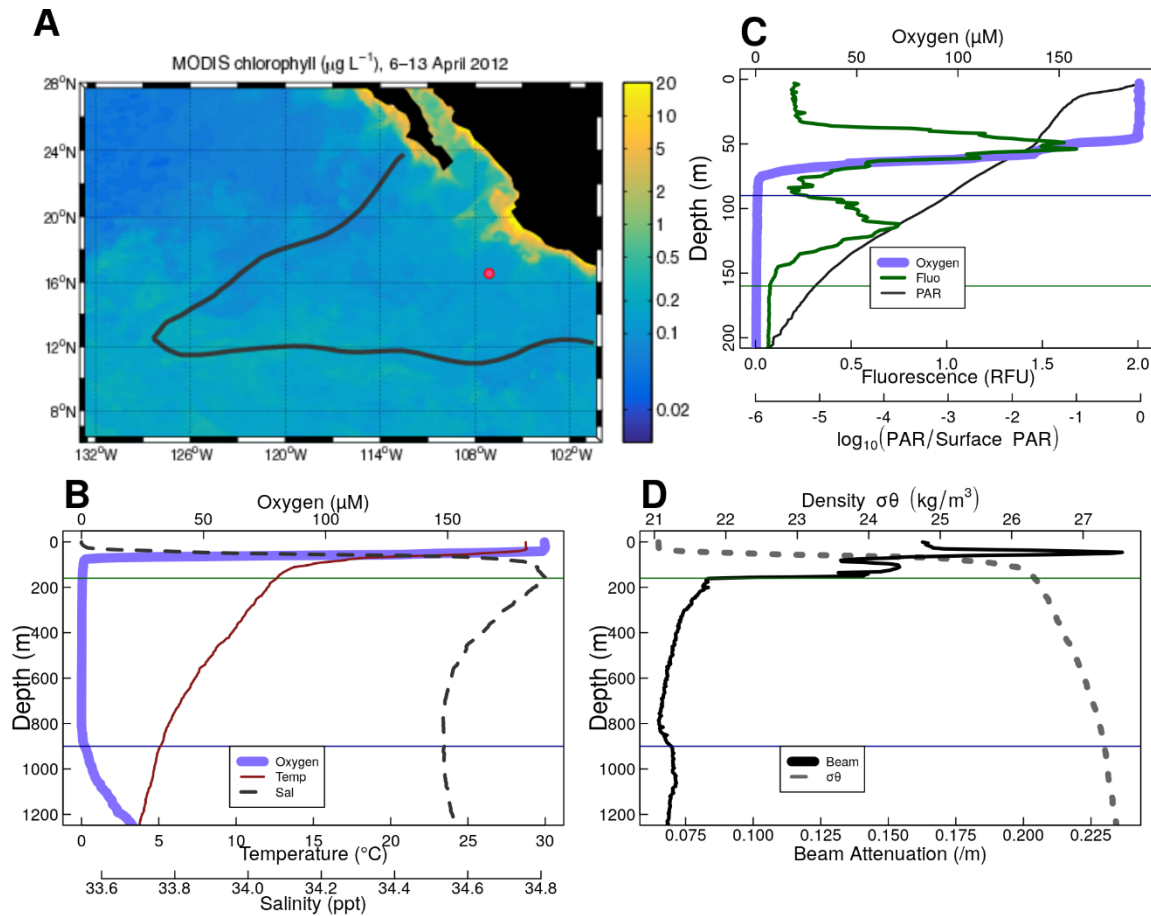
Figure 1. Overview of the geography, physics and chemistry of ETNP Station P2 **A.** Map of the ETNP Oxygen Deficient Zone and the location of Station P2. Colors indicate chlorophyll concentrations at the surface as determined by MODIS satellite in 2012, while the black outline signifies the region containing <10 μM oxygen at 300 m. The red circle indicates the location of Station P2 (modified from Fuchsman et al 2019, credit Hilary Palevsky, Creative Comments License https://creativecommons.org/licenses/by/4.0/). **B-D.** Oceanographic parameters collected from a cast at 2017-01-13 12:15 CST (local time). The thin horizontal green line shows the location of the base of the photic zone (160m B-D), defined by the complete attenuation of the in-situ fluorescence, while the horizontal blue lines show the surface (90 m, C) and base of the ODZ (900m, B,D). **B.** shows temperature, salinity and oxygen. **C.** fluorescence and photosynthetically available radiation (PAR), focusing on the top 200m of the water column and photosynthetically active radiation, and **D.** beam attenuation and density.

12

6.2 Acoustic data reveal diel migration patterns

Acoustic data, produced by the shipboard EK60 (Andersen, 2001), at ETNP Station P2, suggest the presence of multiple cohorts of migratory organisms. We focus initially on backscattering measurements from the EK60's lowest frequency 18000 Hz signal, corresponding to organisms the size of small fish, because it travels furthest into the water column and has the best resolution of the channels. Most migratory organisms appeared to leave the surface at dawn and return at dusk, spending the day between 250 and 500m (Figure 2A). There appeared to be two local maxima in backscattering intensity at mid-day, one at ~300m and one at ~375 m (Figure 2A). There also appeared to be organisms that migrated downward at dusk and upward at dawn, spending the night at ~300m (Figure 2B). There was a peak of organisms that appeared, at mid-day, on some but not all days, without any visible dawn or dusk migration, just above the base of the photic zone. (Figure 2C). Some diel migrators appeared to cross the ODZ and spend the day below the detection range of the EK60 (Figure 2D), as well as organisms that appeared between 500m and 1000m but did not appear to migrate to or from that depth at our site, but rather traveled through the EK60's field of view (Figure 2D).

Similar patterns were evident in each of the other measured frequencies, with better resolution by the lower frequencies (Figure S3).
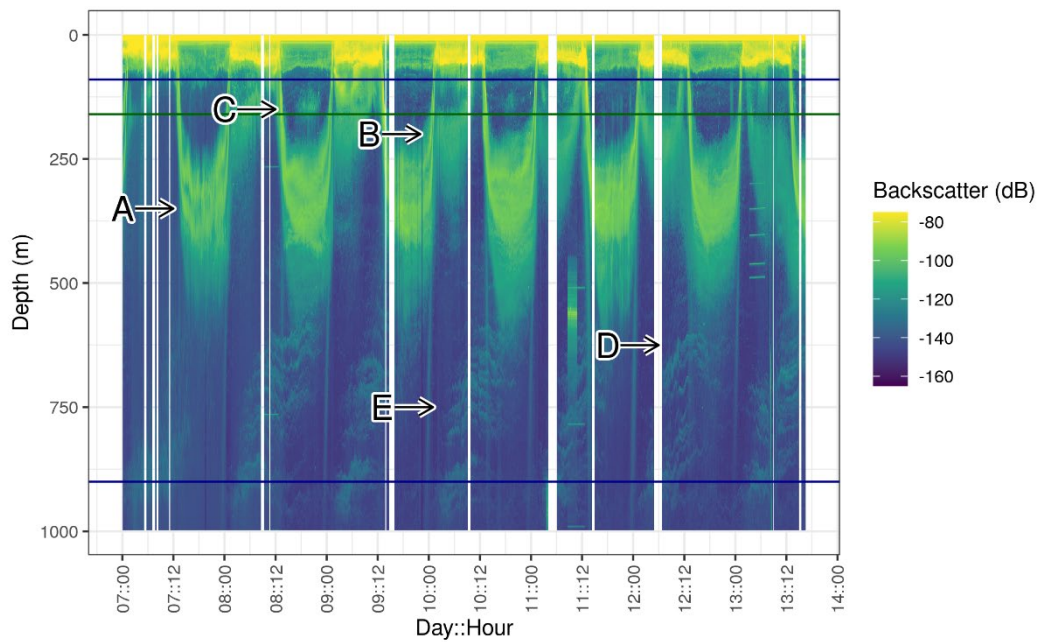

Figure 2. Acoustic data, measured by EK60 over the course of the experiment, at ETNP Station P2. Shown are data from the 18000 Hz frequency band, which have highest depth penetration, but which appear to co-occur with data from other frequency bands (see Figure S3). Values are in return signal intensity and have not been normalized to observed biomass. Horizontal blue

lines indicate the surface and bottom of the ODZ, while the horizontal green line indicates the base of the photic zone. Several patterns can be seen: **A.** Two bands of organisms can be seen leaving the surface at dawn, spending the day between 250 and 500m and returning to the surface at dusk. **B.** Another group of nocturnally migrating organisms can be seen leaving the surface at dusk, spending the night near 250m and returning at dawn. **C.** Some organisms appear at the base of the photic zone, during some, but not all mid days, and then disappear in the evening. **D.** A group of very deep migrating organisms appears to leave the surface with the diel migrators and pass all the way through the ODZ and out of the EK60's field of view. It returns at dusk. **E.** Swarms of organisms appear between 500 and 1000m disappearing later in the day. Swarms appear in the deepest layers at night and appear progressively shallower as the day progresses.

6.3   Flux data from traps

Flux measurements at Station P2 were consistent between the different particle trap types, showing a profile that broadly followed a power law with respect to depth, with the exception that flux appeared to increase in one trap at 500 m (Figure 3).
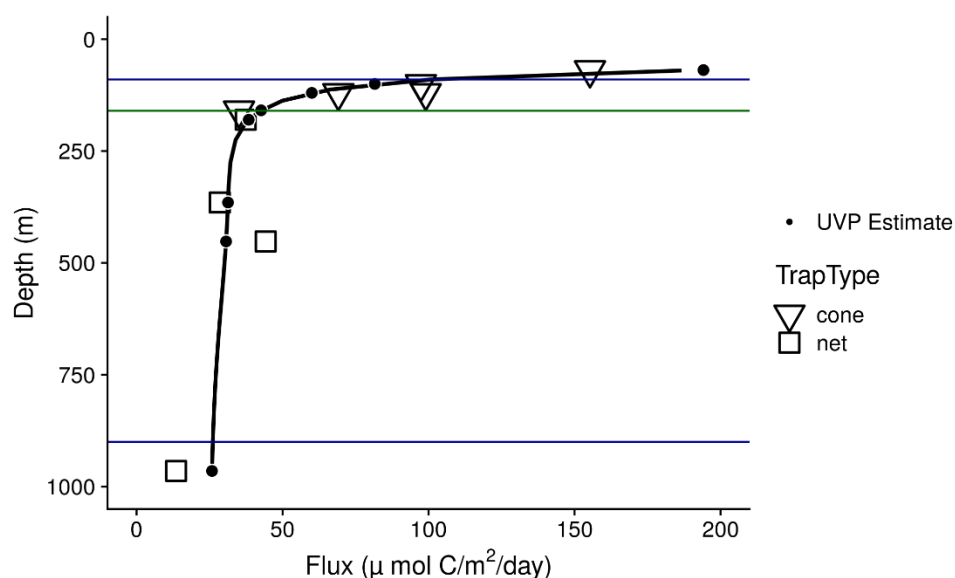

Figure 3. Sinking particle flux, measured from surface-tethered sediment traps (large symbols), at ETNP Station P2. Trap types are shown by the shape of the large points. Superimposed are estimates of particle flux from the UVP generated by fitting the sum of particle numbers all four profiles to the trap observed flux. The black line indicates flux predictions made by fitting UVP observations to the trap data. Black circles indicate regions on the black line corresponding to

14

379   the trap observation depths. Horizontal blue lines indicate the surface and bottom of the ODZ,

380   while the horizontal green line indicates the base of the photic zone.

6.4   Particle abundance measurements vary with size and depth

382   In all profiles, particle abundances were highest at the surface, and highest among the smallest particles

383   (Figure S4). Visual examination of the relationship between particle number and size suggested a power

384   law relationship where the log of volume and bin-size normalized particle abundance was proportional to

385   the log of the particles' size (Figure S5). The exception to this pattern were particles larger than 10 mm

386   (Figure S4, S5), which are rare enough that they are usually not detected by the UVP. Generalized linear

387   models that assume a negative-binomial distribution of the data accounted for this under-sampling of

388   large particles to estimate power law slopes, while considering rare occurrences of the large particles at

389   each depth (Figure S5).

390   Total particle numbers were generally similar between different casts, regardless of which day or hour

391   they were collected (Figure 4A). Particle numbers were highest in the surface and decreased within the

392   oxic region, then remained relatively constant from 160 m to 500 m, and gradually decreased between

393   500 m and the lower oxycline (Figure 4A).

394   The particle size distribution slope generally steepened (became more negative) between the surface and

395   500 m, flattened (became less negative) between 500 m and 1000 m, and then steepened again below

396   1000 m (Figure 4B). Steeper, more negative, slopes indicate a higher proportion of small particles relative

397   to large particles, while flatter, less negative, slopes indicate a higher proportion of large particles.

15
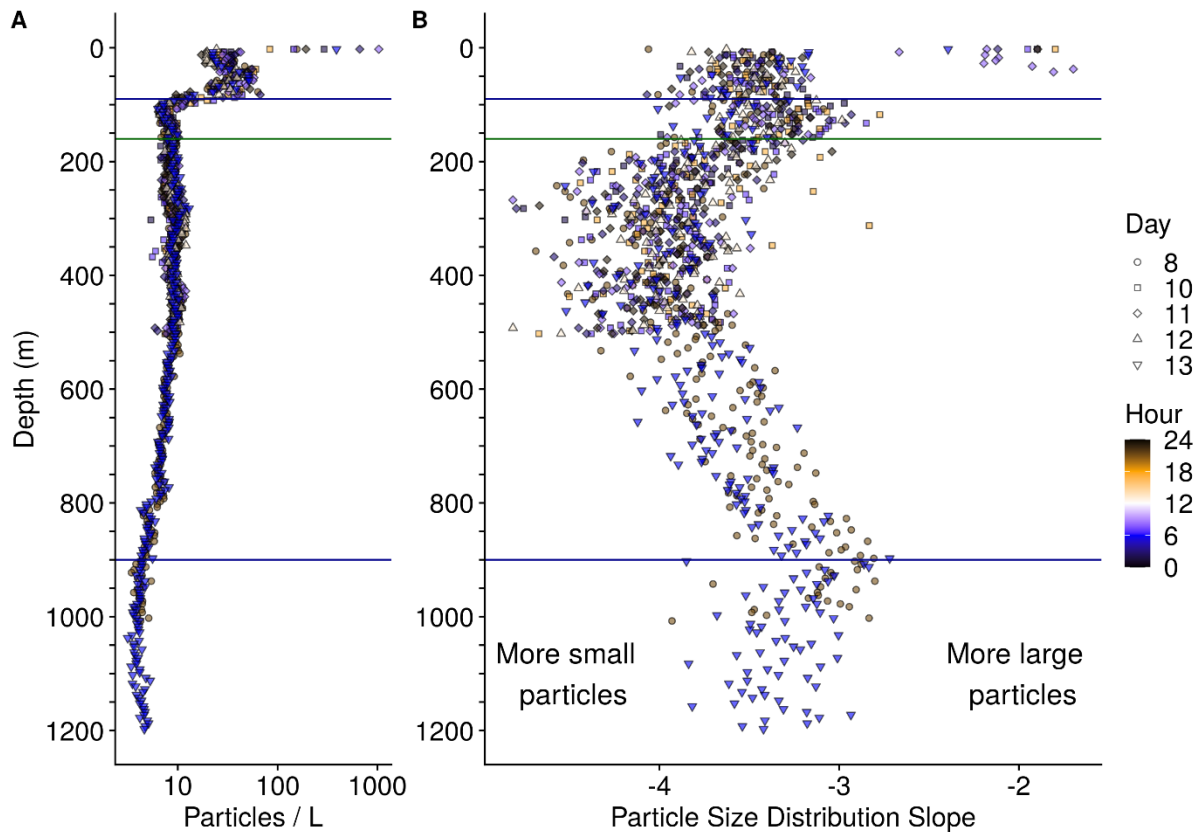
Figure 4. A. Observed, volume normalized total particle numbers from 9 casts taken at different times of the day at ETNP station P2. **B.** Calculated particle size distribution slopes of those particles. These data have not been binned by depth. Horizontal blue lines indicate the surface and bottom of the ODZ, while the horizontal green line indicates the base of the photic zone.

6.5   Estimated particle flux sometimes increases with depth in the ODZ core

Optimization found best agreement between particle flux measured by traps, and UVP estimated particle flux when per particle flux is fit by the equation:

Flux = (133 μ mol C / m^2/day) = **133 * Size (mm) ^ 2.00**   (Eqn 5)

Applying this fit to the UVP data resulted in a UVP predicted flux profile that broadly fit the expected trap observed flux profiles (Figure 3).

Particle flux profiles, predicted from the above particle size abundances and fit, varied between casts between the base of the photic zone and 500 m (Figure 5A-5B). To examine the rate of change of flux and to identify regions and time points where flux appeared to increase with depth, we examined the rate of change of flux. This rate of change was fifth root transformed to normalize the data and to allow us to focus on the cases where flux attenuation varied about zero, since we were interested in identifying

16

414 factors that related to whether flux was positive or negative. Between 250 m and 500 m, particle flux

415 appeared to increase on some, but not all, casts, while attenuating slowly on the other casts (Figure 5C).

416 Below 500 m, there were not enough casts to measure variability between casts.

417 The general additive model that quantified the how the of change of flux between 250 m and 500 m

418 varied with depth, decimal study day and decimal hour found that depth ($p = 0.061$) and hour of the day

419 ($p = 0.196$) did not statistically associate with the fifth root transformed rate of change of flux while day

420 of study did ($p = 0.019$) ($R^2 = 0.264$) (Figure S6). There were generally increases in flux over this region

421 towards the beginning and end of the sampling period and decreases in flux nearer to day 10 (Figure

422 S6B). A general additive model that looked only at the relationship between study day and rate of change

423 of flux (fifth root transformed) in this region suggested that day accounted for 14% of the variance in this

424 value, as determined by adjusted R^2 ($p = 0.040$). If the fifth root transformation was not applied to the

425 rate of change of flux, there was a statistically significant relationship between depth and rate of change

426 ($p = 0.001$), but not study day ($p = 0.062$) or hour ($p = 0.719$) ($R^2 = 0.341$). This pattern indicated that,

427 without the transformation, any temporal signal is swamped by the substantial changes in rate of change

428 in depth, with shallower depths losing flux faster than deeper ones.

17
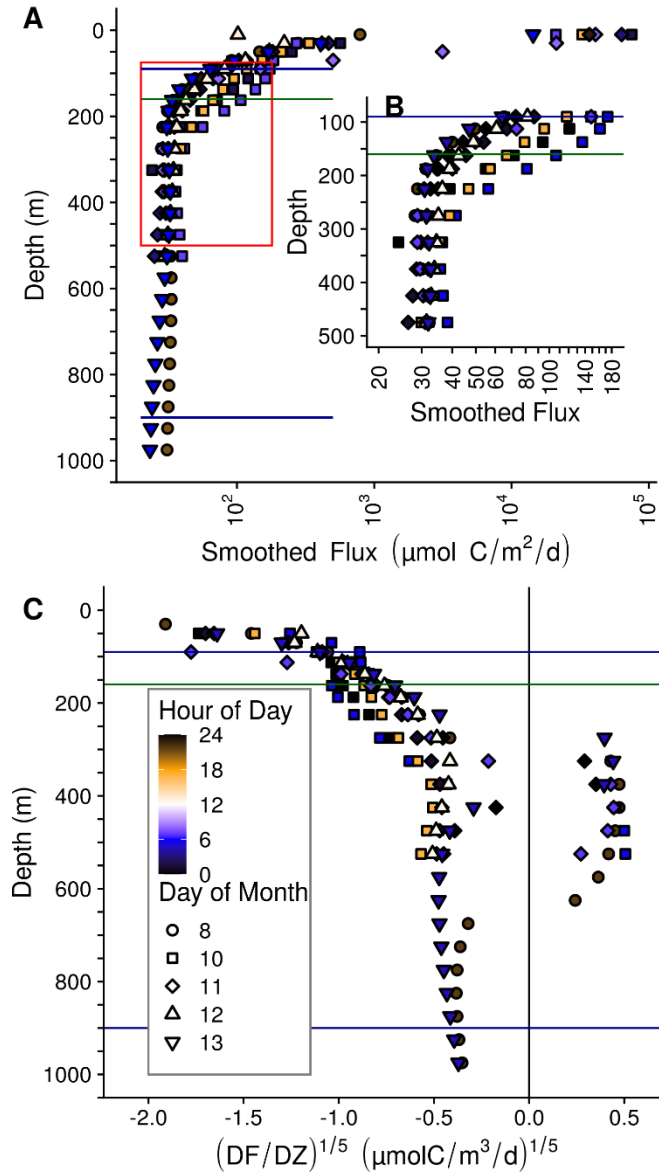
Figure 5. Within and between day variability in UVP predicted particle flux at ETNP Station P2. All profiles are depth binned with higher resolution towards the surface (methods). Horizontal blue lines indicate the surface and bottom of the ODZ, while the horizontal green line indicates the base of the photic zone. **A.** Flux profiles in the top 1000m of the water column. **B.** A more detailed depiction of the area enclosed by the rectangle in **A**. -- **C.** The rate of change of flux, divided by the rate in change in depth. We show the fifth root of these values to highlight differences between values close to zero.

18

6.6 ETNP particle dynamics differ from those seen at an oxic site

The oxic site, P16 Station 100, was characterized by a more gradually sloping pycnocline, and an oxygen minimum at 500 m of 19.7 μM, which is hypoxic (Figure S1B). There was no working fluorescence sensor on that cruise, but data from World Ocean Atlas (Boyer et al., 2018) suggest that the photic zone is characterized by a single fluorescence peak with a maximum at 110 m and which disappeared at 200 m (Figure S1C). Thus we define the mesopelagic as beginning at 200 m at the oxic site. Turbidity followed chlorophyll concentration and did not have a peak in the mesopelagic (Figure S1D), unlike the ODZ site. There was a salinity peak at 150 m (Figure S1B).

Particle numbers were higher, between the base of the photic zone through 1000 m at the ETNP ODZ site, than at the same-latitude, oxygenic P16 Station 100 (Figure S7A). Particle size distributions were similar between the two sites above 500 m, being characterized by overlapping confidence intervals generated by a general additive model. From 500 m to 1000 m, particle size distributions were flatter at the ETNP site, being characterized by a smaller proportion of small particles, relative to large ones (Figure S7B).

Small particles (100 μm - 500 μm) at the ETNP ODZ site were about two orders of magnitude more common than large particles (≥ 500 μm) (Figure S8). Large particle numbers appeared to attenuate more quickly than small particles, and more generally follow a power law decrease, while small particles appeared to increase around 500 m. Flux was predicted to be predominantly from small, rather than large particles, at all depths except the very surface. The particle size distribution, calculated only on large particles, was more variable between depths than calculated for small particles. Data from the oxic P16 Station 100 suggested more particles, steeper particle size distribution, and more flux at this station than at the ETNP station. They also suggested that differences between large and small particles, with respect to number, flux and size distribution that were broadly similar to the ones seen at ETNP Station P2.

In contrast to the anoxic station, at the oxic station, flux always decreased with depth (Figure S9A+B).

6.7 Smoothed and averaged data

Highly smoothed particle abundance data suggested that particle size, averaged across all casts, followed a pattern in which the abundance of small particles increased between the oxycline and 350 m (Figure 6A), which corresponded with steepening of the particle size distribution slope (Figure 6B), and an increase in small particle biomass (Figure 6C), but not of large particle biomass (Figure 6D). Deeper in the ODZ, the small particle number, particle size distribution slope, and biomass of small particles declined. At the oxic site, particle size distributions generally steepened with depth, while both small and large particle estimated biomass followed a power law decrease with depth (Figure S10).
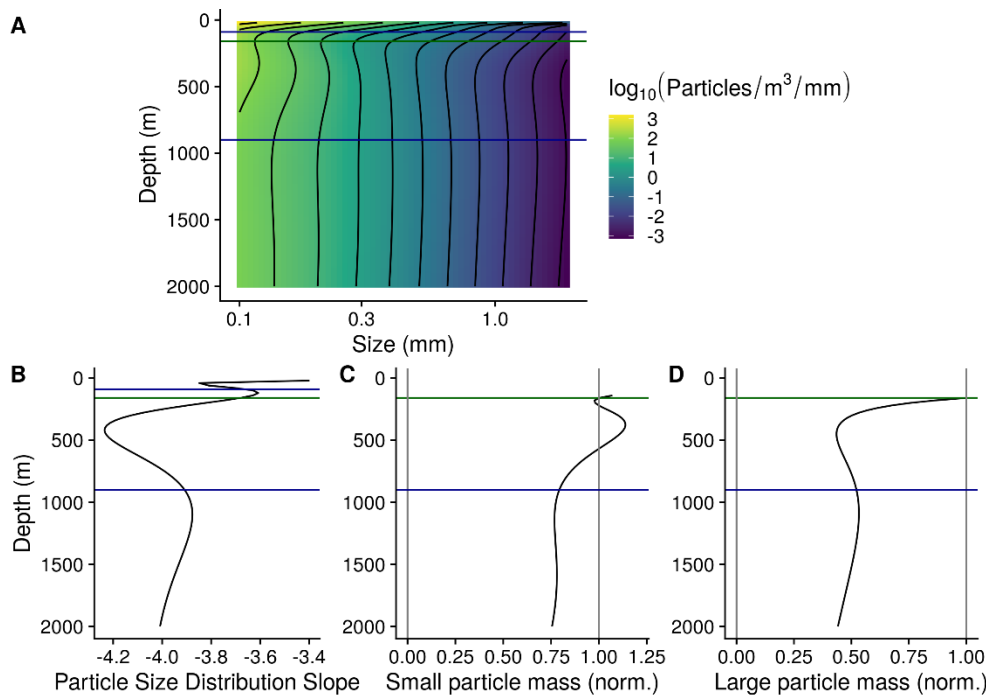
19

Figure 6. A. GAM smoothed, bin-size and volume normalized particle numbers across the particle size spectrum, at ETNP Station P2. Data are from the only cast that traversed the top 2000m of the water column, collected on January 13 beginning at 06:13. Horizontal blue lines indicate the surface and bottom of the ODZ, while the horizontal green line indicates the base of the photic zone. **B.** Particle size distribution slope. **C-D**. Estimated biomass of **(C)** small and **(D)** large particles, normalized to biomass at the base of the photic zone. In these two biomass panels, data from above the base of the photic zone are not shown.

6.8 Particle number dynamics differ from model expectations

The modified particle remineralization and sinking model predicted particle size distributions at each depth from the particle size distribution one depth-bin shallower and the calculated flux attenuation between the two depths. We found that the observed particle size distributions usually deviated from model expectations (Figure S11). In the model, remineralization rates are optimized, to ensure that the total predicted flux at each depth matches the observed total flux. However, the predicted size spectrum will diverge from the observed spectrum if the assumptions of the model (i.e., sinking and remineralization are the only particle transformations) are violated. The difference between the observed and predicted flux of *small particles* ($100 - 500\mu m$), normalized to depth, therefore serves as a metric of observed deviations from the size distribution expected from sinking and remineralization alone. We call this value *Deviation from Model* (DFM).

20

$$487 \quad DFM = \frac{(Small\ Flux\ Observed - Small\ Flux\ Modeled)}{\Delta Z} \qquad \text{(Eqn. 6)}$$

488   In the above equation ΔZ is the distance, in meters, between the current depth bin and the previous depth

489   bin, whose particle size distribution is fed into the predictive model.

490   DFM was positive between the photic zone (160m) and 500 m, meaning that less small flux attenuated

491   than would be expected from the *PRiSM* model in this region (Figure 7). There was some variability in

492   the DFM parameter between casts. A general additive model (GAM) that showed that the variability in

493   DFM was statistically significantly related to depth ($p < 10^{-5}$), day of the study ($p = 0.002$), but not to

494   hour of the day ($p = 0.051$), with these factors together explaining 41.6% of the variance, as measured by

495   R^2. DFM was highest shallower in the water column (Figure S12A), highest near day 10 and lower at the

496   beginning and end of the study (Figure S12B). A GAM that only explored the effect of depth accounted

497   for 27% of the variance. Comparing a GAM that accounted for study day and depth to one that only

498   accounted for depth effects showed an increase in R^2 value of 11%, suggesting that study day accounts for

499   11% of the variance, after accounting for depth. Comparing the model that accounts for depth, day and

500   hour to one that only accounts for depth and day, suggests that hour of the day, while not statistically

501   significant, could explains an additional 3% of the variance.

502   Below 500 m, DFM was negative. There were only two casts that reached below 500m at this station, and

503   so an analysis of the dynamics of DFM in this region is not possible. At P16 Station 100, DFM was

504   positive between the base of the photic zone and 350m and negative below 350 m (Figure S9C).
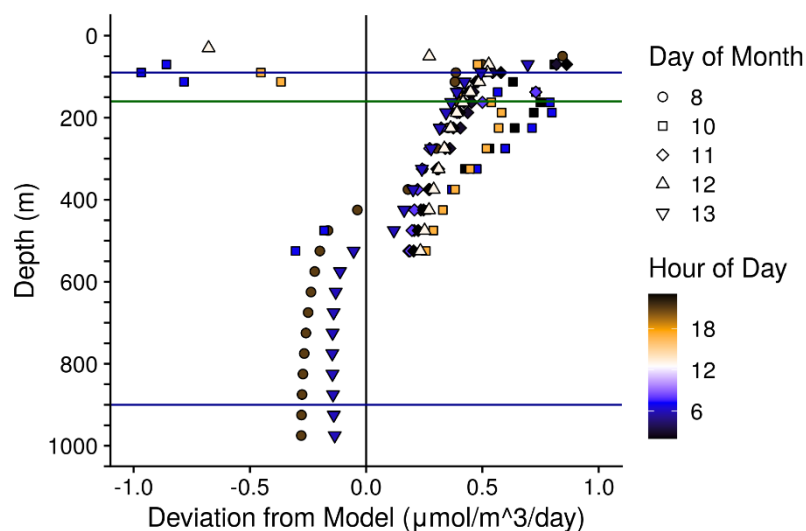

505

506   **Figure 7.** *Deviation from Model (DFM)* indicates the difference between the observed flux of

507   small particles (< 500 μm), and the flux of small particles that would be estimated by a model,

508   which assumes that particles in the depth bin above only remineralized and sank, following the

21

509 PRiSM model. Values are normalized to the change in depth and are in units of μ mol Carbon

510 m^{-3}d^{-1}. This value serves as a metric of disaggregation and other processes, which cannot be

511 captured by a null model that assumes that particles only sink and remineralize. *DFM* is

512 reported for all casts at ETNP Station P2. Horizontal blue lines indicate the surface and bottom

513 of the ODZ, while the horizontal green line indicates the base of the photic zone.

7 *Discussion*

7.1 **Diel migrators spend time in the ODZ core**

516 Organisms of all sizes appear to migrate into the core of the ODZ at our site. Most migrators appear to

517 leave the surface at dawn, spend the day in the top 500 m of the ODZ and return to the surface at dusk

518 (Figure 2A), while others show the opposite pattern, leaving the surface at dusk and returning at dawn

519 (Figure 2B). Diel migration is prevalent throughout the oceans (Cisewski et al., 2010; Hays, 2003;

520 Heywood, 1996; Jiang et al., 2007; Rabindranath et al., 2011; Sainmont et al., 2014; Yang et al., 2019),

521 including at other ODZ sites (Antezana, 2009; Kiko et al., 2020; Riquelme-Bugueño et al., 2020), some

522 of which are highly anoxic sites with secondary, anoxic, deep chlorophyll maxima, like this one (Hidalgo

523 et al., 2005), and much of the ETNP ODZ (Herrera et al., 2019). Sampling efforts elsewhere in the ETNP

524 suggest that many of these diel migrators are euphausiids and fish (Maas et al., 2014; Wishner et al.,

525 2013), and that diel migrators are primarily 2-5 mm in size (Wishner et al., 2013). Krill in the Humboldt

526 current OMZ migrate to the surface at night (Riquelme-Bugueño et al., 2020), as seen for some organisms

527 at our site (Figure 1B). The presence of organisms that appear and disappear just above the base of the

528 photic zone, in the region of the deeper anoxic fluorescence peak region, but absence of a tell-tale

529 signature of mass migration before or after they appear (Figure 1C) may suggest that these organisms

530 migrate at different times of the day to this deep region, rather than all at once. Another possibility is that

531 they pass through our station at this depth in mid-day, but do not migrate to depth at this location, but

532 rather at another location.

533 The organisms that appear between 500 m and 1000 m (Figure 2E) have acoustic signatures that resemble

534 those of jellyfish (Kaartvedt et al., 2007). That they appear in horizontal bands that do not appear to trend

535 upwards over time suggests that jellyfish swarms are traveling through our site at progressively shallower

536 depths over the course of the day, but that the individual swarms are not themselves moving upward at

537 this station. This suggests that any vertical migration by these organisms happens elsewhere or occurs

538 more slowly than the advection seen at this site. That they appear at different depths at different times of

539 the day suggest that these organisms have some sort of vertical migration pattern. Future work may

540 consider more highly resolved spatial and temporal monitoring of this phenomenon. Indeed molecular

22

541 surveys have found evidence of both Cnidarians and Ctenophores both within and below the ETSP ODZ
542 near Chile (Parris et al., 2014).

7.2   Flux is lower at this site than previous measurements in the ETNP

544 Flux at P2 was lower at all depths, ranging from 10-100 $\mu M/m^2/day$, than was seen in previous
545 measurements by traps at other, more productive, ODZ sites, which ranged from 1-10 $mM/m^2/day$
546 (Hartnett & Devol, 2003; Van Mooy et al., 2002).

7.3   The flux to size relationship is typical of other sites

548 The exponent of the particle size to flux relationship that we saw at our site (2.00) is of a similar
549 magnitude to, but slightly smaller than, those seen by other studies that compare UVP flux to trap flux
550 (Guidi et al., 2008; Kiko et al., 2020). Differences in the size-flux relationship could indicate that this
551 relationship truly varies between sites, or that imprecision in flux measurements leads to differences in
552 these values between studies. The single fit and relationship that we carried out does not account for
553 variation in the size to flux ratio across time and depth, nor does it account for differences in particles of
554 different origin. In practice, this value could change over depth and time. Setting up, deploying and
555 retrieving each trap array is a large effort. However, coupled particle flux and size measurements that are
556 more resolved with respect to depth, space or time might allow for further exploration of the
557 spatiotemporal variability of this relationship. In other systems, combined image analysis and gel traps
558 (McDonnell & Buesseler, 2010, 2012) has provided opportunities to explore particle size to flux
559 relationships and how they vary between particle types in more detail.

7.4   Remineralization rates of all particles decrease in the ODZ, but
disaggregation does not

562 Particle size profiles, particle size distribution slopes, and estimated biovolume, averaged across all casts
563 and smoothed, are all similar to the predictions made by Weber and Bianchi's (2020) "Model 1". (Figure
564 5), and therefore our hypothesis **H1**. This suggests that the low oxygen at this site decreases the
565 remineralization rate of all particles, including small ones. It does not support the **HA2** in which
566 disaggregation is suppressed in the ODZ, nor **H3** in which only the very large particles' remineralization
567 is slowed due to sulfate reduction. The data at the oxic site generally conformed to Weber and Bianchi's
568 null model, "Model 0", which was their prediction for particle distributions at oxic sites (2020). However,
569 one difference was that the observed particle size distribution, while essentially constant from the base of
570 the photic zone through 1000 m, appeared to steepen between 1000 m and 2000 m, suggesting an increase
571 in the abundance of small particles, relative to Model 0. This could indicate increased disaggregation in

23

572 this region or horizontal transport of small particles through advection in this region. One possible source
573 of horizontal transport is colloids in a deep iron plume (Homoky et al., 2021; Lam et al., 2020).

7.5 Zooplankton likely transport organic matter into the ODZ core

575 Predicted flux levels sometimes increase between 275 m and 625 m, and at all other times attenuate very
576 slowly in this region. The EK60 data suggest the diel migration of all sizes of organisms to this region,
577 agreeing with previous analysis of copepods collected with nets (Wishner et al., 2020). Taken together,
578 the concurrent intermittent increases in flux with diel migration in the top 500 m suggests that
579 zooplankton are transporting organic matter. That the rate of change in flux with depth suggests some
580 day-to-day variability in this transport. That this rate does not vary statistically significantly between day
581 and night suggests that any diel release of particles is relatively small compared to the particles already
582 present in situ. Indeed, it suggests that particle sinking is slow enough that any particles that are
583 transported to depth during the day are retained at night. Furthermore, nocturnal migrators are likely
584 playing a role in carbon transport which may smooth out any diel signal. Another possibility given that
585 the small magnitude of the day-to-day variability in apparent particle flux, is small is that the zooplankton
586 themselves, which likely make up about 5% of what the UVP counts as particles, may be driving this
587 apparent pattern and that particle flux itself does not vary. More likely, especially given the observation
588 that this flux variability did not track well with the within day backscattering patterns seen by the EK60
589 and the small number of particles that are zooplankton, is that this factor accounts for some, but not all, of
590 the observed variability in flux. An additional source of temporal variability in flux is variation in particle
591 export from the photic zone.

592 Zooplankton are known to also congregate at the lower boundaries of ODZs (Wishner et al., 2018, 2020)
593 and high urea concentrations in the lower oxycline of the ETNP has been suggested to be due to these
594 zooplankton (Widner et al., 2018). Beam attenuation indicates a third peak in the oxycline below the
595 ODZ. We do not see this congregation in the EK60 data. However, it is possible that small organisms do
596 congregate here, but are not detected by the EK60's 12000 and 20000 kHZ signals, which do not
597 penetrate to 1000 m in our data. The EK60 data do however suggest that larger, krill to fish sized
598 organisms are not abundant in the lower oxycline. Alternatively, the beam attenuation signal could have a
599 non-zooplankton source, such as in-situ formation by chemoautotrophic processes or horizontal advection
600 of small particles.

7.6 Zooplankton likely disaggregate particles in the ODZ core

602 The observation that there is greater flux by small particles (< 500 μm) than would be predicted by
603 remineralization and sinking alone (Figure 7), between the photic zone and 500 m suggests that some

24

604 process is disaggregating large particles into smaller ones. That this apparent disaggregation corresponds
605 with the region where migratory organisms are found suggests that some of these organisms, likely small
606 animals such as copepods and euphausiids (Herrera et al., 2019; Maas et al., 2014), may break down
607 particles (Dilling & Alldredge, 2000; Goldthwait et al., 2005). While other processes such as horizontal
608 advection of water containing small particles (Inthorn, 2005) could be responsible for this increase in
609 small particles in principle, there is no reason to expect horizontal differences at this site, which is at the
610 core of the ODZ and far from shore.

611 Other deviations from model assumptions could also explain the increase in small particles relative to
612 model predictions. In particular, small particles might break down more slowly than large ones, or sink
613 more quickly for their size than expected, as has been seen elsewhere (McDonnell & Buesseler, 2010).
614 Our model assumes a spherical particle drag profile, such that the particle sinking speed fractal dimension
615 (γ) is one less than the particle size fractal dimension (α) (Cram et al., 2018; Guidi et al., 2008), and that
616 these two values sum to the particle flux fractal dimension. If any of these assumptions do not hold, the
617 magnitude of the values may differ.

618 In contrast to the upper ODZ core, there is an apparent flattening of the particle size distribution below
619 500 m, beyond the expected effects generated by particle remineralization. This could suggest
620 aggregation processes (Burd & Jackson, 2009). Indeed, aggregation could be occurring throughout the
621 ODZ core, but only exceed disaggregation in the lower ODZ region. Alternatively, in this region,
622 processes resembling Weber and Bianchi's (2020) Model 3, corresponding to **H3**, in which large particles
623 remineralize slower than larger ones could also be occurring. Like aggregation, this process could be
624 occurring through the ODZ but is overwhelmed by the effects of disaggregation above 500 m.

625 ## 7.7   Water mass changes may affect particle flux and size changes

626 The observation that particle flux begins to attenuate below 500 m more quickly than it does between the
627 base of the photic zone and 500 m could be explained in part by a shift in water mass at this depth where
628 AAIW begins to mix with NEPIW (Figure S2). The AAIW is suggested to have micromolar oxygen
629 concentrations, as compared to the NEPIW, such that a small contribution of AAIW can raise the oxygen
630 concentration. These conclusions are based on iodine oxidation state proxy data, likely as a result of
631 having a different history than the overlying waters in which less organic matter has remineralized in this
632 water mass by the time it reaches the ETNP (Evans et al., 2020). However, measurements taken at this
633 station in 2012 observed zero oxygen though 800 m with the highly sensitive STOX electrode, suggesting
634 that oxygen, if present, is below 2 nM (Tiano et al., 2014). It is conceivable that the AAIW has larger
635 particle sizes and lower particle abundance characteristics due to its having advected from different
636 geographic regions than the overlying water, but it is difficult to see why this would be the case as these

25

water masses stay in the ODZ region for years (DeVries et al., 2012) and particles have a much shorter residence time. In any case, the NEPIW to AAIW transition coincides with the lower limit of the depth to which vertically migrating zooplankton travel (Figure 2), and so we are not able to deconvolve the effects of water mass changes from that of changes in zooplankton effects on particle characteristics. The zooplankton at our site may be using water mass characteristics, such as temperature or salinity, to determine their migration depths.

The change in water mass between 13CW and NEPIW, around 250 m, in contrast, does not appear to correspond to any apparent changes in particle flux or size. Thus, we would argue that any historical effects of these water mass differences are likely to be small, and that active transport differences above and below 500 m likely have a larger effect.

7.8   Opportunities for future directions

Due to the relatively small effect sizes of day to day and within day variability in particle flux and disaggregation, we advocate for applying these sorts of analysis and measurements to other parts of the ETNP or other ODZ regions, even ones where there are not time-series data. Expanded spatial analysis of particle size spectra in ODZs would allow the community to confirm whether Weber and Bianchi's (2020) model **(H1)**, that particles of all sizes break down more slowly in ODZs, applies elsewhere. Similarly, a clear next step is to apply our disaggregation model to other ocean regions, perhaps using particle size data are already collected by other groups (Guidi et al., 2008; Kiko et al., 2017, 2020).

8   *Conclusions*

If ODZs expand in response to the changing climate, larger areas of the ocean are likely to resemble this environment, which is oligotrophic and has an oxygen deficient zone spanning most of the mesopelagic zone. Previous models and observations have suggested that ODZs are sites of efficient carbon transfer to the deep ocean (Cram et al., 2018; Hartnett & Devol, 2003; Van Mooy et al., 2002; Weber & Bianchi, 2020), and our data appear to support this contention. Indeed, the mechanism of efficient transfer appears to be slowing of particle remineralization, presumably from decreased microbial metabolisms, with zooplankton playing an important role in both active particle transport and particle disaggregation.

Our data could potentially be used in conjunction with mechanistic models (e.g. Weber & Bianchi, 2020) to constrain the relative carbon oxidation rate by denitrification and sulfate reduction processes, which is currently poorly understood (Bristow, 2018). Furthermore, it appears that diel migratory organisms both disaggregate particles and transport carbon throughout the top 500 m of the water column. Day-to-day and within day variability in organic matter transport was evident, though overall patterns in particle size, flux and disaggregation appeared to be consistent over the course of the time-series. The change in

26

particle abundance and size between 500 m and the bottom of the ODZ has implications for the free-living microbes living in this region. These microbes are likely particularly organic matter starved, and so these decaying particles are likely an important energy source for them. Our data highlights the heterogeneous nature of the ETNP ODZ with depth and indicates that more detailed sampling should be performed for rate and microbial measurements to properly extrapolate to the entire ODZ.

9 Acknowledgements

Data for this research, as well as analysis and model code are available on GitHub at https://github.com/cramjaco/POMZ-ETNP-UVP-2017, and are mirrored to FigShare at https://figshare.com/articles/software/POMZ-ETNP-UVP-2017/14589435.

10 References

Andersen, L. N. (2001). The new Simrad EK60 scientific echo sounder system. *The Journal of the Acoustical Society of America*, *109*(5), 2336–2336. https://doi.org/10.1121/1.4744207

Antezana, T. (2009). Species-specific patterns of diel migration into the Oxygen Minimum Zone by euphausiids in the Humboldt Current Ecosystem. *Progress in Oceanography*, *83*(1), 228–236. https://doi.org/10.1016/j.pocean.2009.07.039

Archibald, K. M., Siegel, D. A., & Doney, S. C. (2019). Modeling the Impact of Zooplankton Diel Vertical Migration on the Carbon Export Flux of the Biological Pump. *Global Biogeochemical Cycles*, *33*(2), 181–199. https://doi.org/10.1029/2018GB005983

Bianchi, D., Stock, C., Galbraith, E. D., & Sarmiento, J. L. (2013). Diel vertical migration: Ecological controls and impacts on the biological pump in a one-dimensional ocean model. *Global Biogeochemical Cycles*, *27*(2), 478–491. https://doi.org/10.1002/gbc.20031

Bianchi, D., Weber, T. S., Kiko, R., & Deutsch, C. (2018). Global niche of marine anaerobic metabolisms expanded by particle microenvironments. *Nature Geoscience*, *11*(4), 263. https://doi.org/10.1038/s41561-018-0081-0

Boyer, T., Garcia, H. E., Locarini, R. A., Ricardo, A., Zweng, M. M., Mishonov, A. V., et al. (2018). *World Ocean Atlas 2018.* NOAA National Centers for Environmntal Information.

Briggs, N., Dall'Olmo, G., & Claustre, H. (2020). Major role of particle fragmentation in regulating biological sequestration of CO2 by the oceans. *Science*, *367*(6479), 791–793. https://doi.org/10.1126/science.aay1790

Bristow, L. A. (2018). Anoxia in the snow. *Nature Geoscience*, *11*(4), 226–227. https://doi.org/10.1038/s41561-018-0088-6

Buonassissi, C. J., & Dierssen, H. M. (2010). A regional comparison of particle size distributions and the power law approximation in oceanic and estuarine surface waters. *Journal of Geophysical Research: Oceans*, *115*(C10). https://doi.org/10.1029/2010JC006256

28

710   Burd, A. B., & Jackson, G. A. (2009). Particle Aggregation. *Annual Review of Marine Science*, *1*(1), 65–

711   90. https://doi.org/10.1146/annurev.marine.010908.163904

712   Cavan, E. L., Trimmer, M., Shelley, F., & Sanders, R. (2017). Remineralization of particulate organic

713   carbon in an ocean oxygen minimum zone. *Nature Communications*, *8*, 14847.

714   https://doi.org/10.1038/ncomms14847

715   Cisewski, B., Strass, V. H., Rhein, M., & Krägefsky, S. (2010). Seasonal variation of diel vertical

716   migration of zooplankton from ADCP backscatter time series data in the Lazarev Sea, Antarctica.

717   *Deep Sea Research Part I: Oceanographic Research Papers*, *57*(1), 78–94.

718   https://doi.org/10.1016/j.dsr.2009.10.005

719   Cram, J. A., Weber, T., Leung, S. W., McDonnell, A. M. P., Liang, J.-H., & Deutsch, C. (2018). The Role

720   of Particle Size, Ballast, Temperature, and Oxygen in the Sinking Flux to the Deep Sea. *Global*

721   *Biogeochemical Cycles*, *32*(5), 858–876. https://doi.org/10.1029/2017GB005710

722   Date, S. (2020, November 21). Generalized Linear Models. Retrieved May 2, 2021, from

723   https://towardsdatascience.com/generalized-linear-models-9ec4dfe3dc3f

724   Deutsch, C., Berelson, W., Thunell, R., Weber, T., Tems, C., McManus, J., et al. (2014). Centennial

725   changes in North Pacific anoxia linked to tropical trade winds. *Science*, *345*(6197), 665–668.

726   https://doi.org/10.1126/science.1252332

727   DeVries, T., & Weber, T. (2017). The export and fate of organic matter in the ocean: New constraints

728   from combining satellite and oceanographic tracer observations. *Global Biogeochemical Cycles*,

729   2016GB005551. https://doi.org/10.1002/2016GB005551

730   DeVries, T., Deutsch, C., Primeau, F., Chang, B., & Devol, A. (2012). Global rates of water-column

731   denitrification derived from nitrogen gas measurements. *Nature Geoscience*, *5*(8), 547–550.

732   https://doi.org/10.1038/ngeo1515

733   DeVries, T., Liang, J.-H., & Deutsch, C. (2014). A mechanistic particle flux model applied to the oceanic

734   phosphorus cycle. *Biogeosciences Discuss.*, *11*(3), 3653–3699. https://doi.org/10.5194/bgd-11-

735   3653-2014

736 Dilling, L., & Alldredge, A. L. (2000). Fragmentation of marine snow by swimming macrozooplankton:

737   A new process impacting carbon cycling in the sea. *Deep Sea Research Part I: Oceanographic*

738   *Research Papers*, *47*(7), 1227–1245. https://doi.org/10.1016/S0967-0637(99)00105-3

739 Durkin, C. A., Estapa, M. L., & Buesseler, K. O. (2015). Observations of carbon export by small sinking

740   particles in the upper mesopelagic. *Marine Chemistry*, *175*, 72–81.

741   https://doi.org/10.1016/j.marchem.2015.02.011

742 Evans, N., Boles, E., Kwiecinski, J. V., Mullen, S., Wolf, M., Devol, A. H., et al. (2020). The role of

743   water masses in shaping the distribution of redox active compounds in the Eastern Tropical North

744   Pacific oxygen deficient zone and influencing low oxygen concentrations in the eastern Pacific

745   Ocean. *Limnology and Oceanography*, *65*(8), 1688–1705. https://doi.org/10.1002/lno.11412

746 Francois, R., Honjo, S., Krishfield, R., & Manganini, S. (2002). Factors controlling the flux of organic

747   carbon to the bathypelagic zone of the ocean. *Global Biogeochemical Cycles*, *16*(4), 34-1-34–20.

748   https://doi.org/10.1029/2001GB001722

749 Fuchsman, C. A., Devol, A. H., Saunders, J. K., McKay, C., & Rocap, G. (2017). Niche Partitioning of

750   the N Cycling Microbial Community of an Offshore Oxygen Deficient Zone. *Frontiers in*

751   *Microbiology*, *8*. https://doi.org/10.3389/fmicb.2017.02384

752 Fuchsman, C. A., Palevsky, H. I., Widner, B., Duffy, M., Carlson, M. C. G., Neibauer, J. A., et al. (2019).

753   Cyanobacteria and cyanophage contributions to carbon and nitrogen cycling in an oligotrophic

754   oxygen-deficient zone. *The ISME Journal*, 1. https://doi.org/10.1038/s41396-019-0452-6

755 Garcia-Robledo, E., Padilla, C. C., Aldunate, M., Stewart, F. J., Ulloa, O., Paulmier, A., et al. (2017).

756   Cryptic oxygen cycling in anoxic marine zones. *Proceedings of the National Academy of*

757   *Sciences*, *114*(31), 8319–8324. https://doi.org/10.1073/pnas.1619844114

758 Gilly, W. F., Beman, J. M., Litvin, S. Y., & Robison, B. H. (2013). Oceanographic and Biological Effects

759   of Shoaling of the Oxygen Minimum Zone. *Annual Review of Marine Science*, *5*(1), 393–420.

760   https://doi.org/10.1146/annurev-marine-120710-100849

761 Goldthwait, S. A., Carlson, C. A., Henderson, G. K., & Alldredge, A. L. (2005). Effects of physical

762   fragmentation on remineralization of marine snow. *Marine Ecology Progress Series*, *305*, 59–65.

763 Guidi, L., Jackson, G. A., Stemmann, L., Miquel, J. C., Picheral, M., & Gorsky, G. (2008). Relationship

764   between particle size distribution and flux in the mesopelagic zone. *Deep Sea Research Part I:*

765   *Oceanographic Research Papers*, *55*(10), 1364–1374. https://doi.org/10.1016/j.dsr.2008.05.014

766 Hannides, C. C. S., Landry, M. R., Benitez-Nelson, C. R., Styles, R. M., Montoya, J. P., & Karl, D. M.

767   (2009). Export stoichiometry and migrant-mediated flux of phosphorus in the North Pacific

768   Subtropical Gyre. *Deep Sea Research Part I: Oceanographic Research Papers*, *56*(1), 73–88.

769   https://doi.org/10.1016/j.dsr.2008.08.003

770 Hartnett, H. E., & Devol, A. H. (2003). Role of a strong oxygen-deficient zone in the preservation and

771   degradation of organic matter: a carbon budget for the continental margins of northwest Mexico

772   and Washington State. *Geochimica et Cosmochimica Acta*, *67*(2), 247–264.

773   https://doi.org/10.1016/S0016-7037(02)01076-1

774 Hays, G. C. (2003). A review of the adaptive significance and ecosystem consequences of zooplankton

775   diel vertical migrations. In M. B. Jones, A. Ingólfsson, E. Ólafsson, G. V. Helgason, K.

776   Gunnarsson, & J. Svavarsson (Eds.), *Migrations and Dispersal of Marine Organisms* (pp. 163–

777   170). Dordrecht: Springer Netherlands. https://doi.org/10.1007/978-94-017-2276-6_18

778 Herrera, I., Yebra, L., Antezana, T., Giraldo, A., Färber-Lorda, J., & Hernández-León, S. (2019). Vertical

779   variability of Euphausia distinguenda metabolic rates during diel migration into the oxygen

780   minimum zone of the Eastern Tropical Pacific off Mexico. *Journal of Plankton Research*, *41*(2),

781   165–176. https://doi.org/10.1093/plankt/fbz004

782 Heywood, K. J. (1996). Diel vertical migration of zooplankton in the Northeast Atlantic. *Journal of*

783   *Plankton Research*, *18*(2), 163–184. https://doi.org/10.1093/plankt/18.2.163

784 Hidalgo, P., Escribano, R., & Morales, C. E. (2005). Ontogenetic vertical distribution and diel migration

785   of the copepod Eucalanus inermis in the oxygen minimum zone off northern Chile (20–21° S).

786   *Journal of Plankton Research*, *27*(6), 519–529. https://doi.org/10.1093/plankt/fbi025

787   Homoky, W. B., Conway, T. M., John, S. G., König, D., Deng, F., Tagliabue, A., & Mills, R. A. (2021).

788   Iron colloids dominate sedimentary supply to the ocean interior. *Proceedings of the National*

789   *Academy of Sciences*, *118*(13), e2016078118. https://doi.org/10.1073/pnas.2016078118

790   Horak, R. E. A., Ruef, W., Ward, B. B., & Devol, A. H. (2016). Expansion of denitrification and anoxia

791   in the eastern tropical North Pacific from 1972 to 2012. *Geophysical Research Letters*, *43*(10),

792   2016GL068871. https://doi.org/10.1002/2016GL068871

793   Inthorn, M. (2005). Lateral particle transport in nepheloid layers - a key factor for organic matter

794   distribution and quality in the Benguela high-productivity area. Retrieved from

795   https://media.suub.uni-bremen.de/handle/elib/2212

796   Ito, T., Minobe, S., Long, M. C., & Deutsch, C. (2017). Upper ocean O_2 trends: 1958-2015. *Geophysical*

797   *Research Letters*, *44*(9), 4214–4223. https://doi.org/10.1002/2017GL073613

798   Jackson, G. A., & Burd, A. B. (2001). A model for the distribution of particle flux in the mid-water

799   column controlled by subsurface biotic interactions. *Deep Sea Research Part II: Topical Studies*

800   *in Oceanography*, *49*(1), 193–217. https://doi.org/10.1016/S0967-0645(01)00100-X

801   Jiang, S., Dickey, T. D., Steinberg, D. K., & Madin, L. P. (2007). Temporal variability of zooplankton

802   biomass from ADCP backscatter time series data at the Bermuda Testbed Mooring site. *Deep Sea*

803   *Research Part I: Oceanographic Research Papers*, *54*(4), 608–636.

804   https://doi.org/10.1016/j.dsr.2006.12.011

805   Kaartvedt, S., Klevjer, T. A., Torgersen, T., Sørnes, T. A., & Røstad, A. (2007). Diel vertical migration of

806   individual jellyfish (Periphylla periphylla). *Limnology and Oceanography*, *52*(3), 975–983.

807   https://doi.org/10.4319/lo.2007.52.3.0975

808   Keil, R. G., Neibauer, J. A., & Devol, A. H. (2016). A multiproxy approach to understanding the

809   "enhanced" flux of organic matter through the oxygen-deficient waters of the Arabian Sea.

810   *Biogeosciences*, *13*(7), 2077–2092. http://dx.doi.org/10.5194/bg-13-2077-2016

811   Kiko, R., Biastoch, A., Brandt, P., Cravatte, S., Hauss, H., Hummels, R., et al. (2017). Biological and

812   physical influences on marine snowfall at the equator. *Nature Geoscience*, *10*(11), 852–858.

813   https://doi.org/10.1038/ngeo3042

814   Kiko, R., Brandt, P., Christiansen, S., Faustmann, J., Kriest, I., Rodrigues, E., et al. (2020). Zooplankton-

815   Mediated Fluxes in the Eastern Tropical North Atlantic. *Frontiers in Marine Science*, *7*.

816   https://doi.org/10.3389/fmars.2020.00358

817   Kwon, E. Y., & Primeau, F. (2008). Optimization and sensitivity of a global biogeochemistry ocean

818   model using combined in situ DIC, alkalinity, and phosphate data. *Journal of Geophysical*

819   *Research: Oceans*, *113*(C8), C08011. https://doi.org/10.1029/2007JC004520

820   Lam, P., & Kuypers, M. M. M. (2011). Microbial Nitrogen Cycling Processes in Oxygen Minimum

821   Zones. *Annual Review of Marine Science*, *3*(1), 317–345. https://doi.org/10.1146/annurev-marine-

822   120709-142814

823   Lam, P. J., Heller, M. I., Lerner, P. E., Moffett, J. W., & Buck, K. N. (2020). Unexpected Source and

824   Transport of Iron from the Deep Peru Margin. *ACS Earth and Space Chemistry*, *4*(7), 977–992.

825   https://doi.org/10.1021/acsearthspacechem.0c00066

826   Maas, A. E., Frazar, S. L., Outram, D. M., Seibel, B. A., & Wishner, K. F. (2014). Fine-scale vertical

827   distribution of macroplankton and micronekton in the Eastern Tropical North Pacific in

828   association with an oxygen minimum zone. *Journal of Plankton Research*, *36*(6), 1557–1575.

829   https://doi.org/10.1093/plankt/fbu077

830   McDonnell, A. M. P., & Buesseler, K. O. (2010). Variability in the average sinking velocity of marine

831   particles. *Limnology and Oceanography*, *55*(5), 2085–2096.

832   https://doi.org/10.4319/lo.2010.55.5.2085

833   McDonnell, A. M. P., & Buesseler, K. O. (2012). A new method for the estimation of sinking particle

834   fluxes from measurements of the particle size distribution, average sinking velocity, and carbon

835   content. *Limnology and Oceanography: Methods*, *10*(5), 329–346.

836   https://doi.org/10.4319/lom.2012.10.329

837   Neuer, S., Iversen, M., & Fischer, G. (2014). The Ocean's Biological Carbon pump as part of the global

838   Carbon Cycle. *Limnology and Oceanography E-Lectures*, *4*(4), 1–51.

839   https://doi.org/10.4319/lol.2014.sneuer.miversen.gfischer.9

840   Ooi, H. (2013, August 8). Where does the offset go in Poisson/negative binomial regression? Retrieved

841   May 2, 2021, from https://stats.stackexchange.com/questions/66791/where-does-the-offset-go-in-

842   poisson-negative-binomial-regression

843   Parris, D. J., Ganesh, S., Edgcomb, V. P., DeLong, E. F., & Stewart, F. J. (2014). Microbial eukaryote

844   diversity in the marine oxygen minimum zone off northern Chile. *Frontiers in Microbiology*, *5*.

845   https://doi.org/10.3389/fmicb.2014.00543

846   Passow, U., & Carlson, C. (2012). The biological pump in a high CO2 world. *Marine Ecology Progress*

847   *Series*, *470*, 249–271. https://doi.org/10.3354/meps09985

848   Pavia, F. J., Anderson, R. F., Lam, P. J., Cael, B. B., Vivancos, S. M., Fleisher, M. Q., et al. (2019).

849   Shallow particulate organic carbon regeneration in the South Pacific Ocean. *Proceedings of the*

850   *National Academy of Sciences*, *116*(20), 9753–9758. https://doi.org/10.1073/pnas.1901863116

851   Pennington, J. T., Mahoney, K. L., Kuwahara, V. S., Kolber, D. D., Calienes, R., & Chavez, F. P. (2006).

852   Primary production in the eastern tropical Pacific: A review. *Progress in Oceanography*, *69*(2–4),

853   285–317. https://doi.org/10.1016/j.pocean.2006.03.012

854   Peterson, M. L., Wakeham, S. G., Lee, C., Askea, M. A., & Miquel, J. C. (2005). Novel techniques for

855   collection of sinking particles in the ocean and determining their settling rates. *Limnology and*

856   *Oceanography: Methods*, *3*(12), 520–532. https://doi.org/10.4319/lom.2005.3.520

857   Picheral, M., Guidi, L., Stemmann, L., Karl, D. M., Iddaoud, G., & Gorsky, G. (2010). The Underwater

858   Vision Profiler 5: An advanced instrument for high spatial resolution studies of particle size

859   spectra and zooplankton. *Limnology and Oceanography: Methods*, *8*(9), 462–473.

860   https://doi.org/10.4319/lom.2010.8.462

861   Picheral, M., Colin, S., & Irisson, J.-O. (2017). *EcoTaxa, a tool for the taxonomic classification of*

862   *images.* Retrieved from http://ecotaxa.obs-vlfr.fr

34

863   Rabindranath, A., Daase, M., Falk-Petersen, S., Wold, A., Wallace, M. I., Berge, J., & Brierley, A. S.

864   (2011). Seasonal and diel vertical migration of zooplankton in the High Arctic during the autumn

865   midnight sun of 2008. *Marine Biodiversity*, *41*(3), 365–382. https://doi.org/10.1007/s12526-010-

866   0067-7

867   Raven, M. R., Keil, R. G., & Webb, S. M. (2021). Microbial sulfate reduction and organic sulfur

868   formation in sinking marine particles. *Science*, *371*(6525), 178–181.

869   https://doi.org/10.1126/science.abc6035

870   Riquelme-Bugueño, R., Pérez-Santos, I., Alegría, N., Vargas, C. A., Urbina, M. A., & Escribano, R.

871   (2020). Diel vertical migration into anoxic and high- p CO 2 waters: acoustic and net-based krill

872   observations in the Humboldt Current. *Scientific Reports*, *10*(1), 17181.

873   https://doi.org/10.1038/s41598-020-73702-z

874   Rocap, G., Keil, R., Devol, A., & Deutsch, C. (2017). Water temperature, salinity, and other data from

875   CTD taken from the RV Sikuliaq in the Pacific Ocean between San Diego, California and

876   Manzanillo, Mexico from 2016-12-21 to 2017-01-13 (NCEI Accession 0164968). [Temperature,

877   Salinity, Oxygen, Beam Attenuation, Fluorescence, PAR]. NOAA National Centers for

878   Environmental Information. Retrieved from https://accession.nodc.noaa.gov/0164968

879   Roullier, F., Berline, L., Guidi, L., Durrieu De Madron, X., Picheral, M., Sciandra, A., et al. (2014).

880   Particle size distribution and estimated carbon flux across the Arabian Sea oxygen minimum

881   zone. *Biogeosciences*, *11*(16), 4541–4557. https://doi.org/10.5194/bg-11-4541-2014

882   Sainmont, J., Gislason, A., Heuschele, J., Webster, C. N., Sylvander, P., Wang, M., & Varpe, Ø. (2014).

883   Inter- and intra-specific diurnal habitat selection of zooplankton during the spring bloom

884   observed by Video Plankton Recorder. *Marine Biology*, *161*(8), 1931–1941.

885   https://doi.org/10.1007/s00227-014-2475-x

886   Saunders, J. K., Fuchsman, C. A., McKay, C., & Rocap, G. (2019). Complete arsenic-based respiratory

887   cycle in the marine microbial communities of pelagic oxygen-deficient zones. *Proceedings of the*

888   *National Academy of Sciences*, *116*(20), 9925–9930. https://doi.org/10.1073/pnas.1818349116

889   Schmidtko, S., Stramma, L., & Visbeck, M. (2017). Decline in global oceanic oxygen content during the

890   past five decades. *Nature*, *542*(7641), 335–341. https://doi.org/10.1038/nature21399

891   Siegel, D. A., Buesseler, K. O., Behrenfeld, M. J., Benitez-Nelson, C. R., Boss, E., Brzezinski, M. A., et

892   al. (2016). Prediction of the Export and Fate of Global Ocean Net Primary Production: The

893   EXPORTS Science Plan. *Frontiers in Marine Science*, *3*.

894   https://doi.org/10.3389/fmars.2016.00022

895   Simon, M., Grossart, H., Schweitzer, B., & Ploug, H. (2002). Microbial ecology of organic aggregates in

896   aquatic ecosystems. *Aquatic Microbial Ecology*, *28*(2), 175–211.

897   https://doi.org/10.3354/ame028175

898   Steinberg, D. K., & Landry, M. R. (2017). Zooplankton and the Ocean Carbon Cycle. *Annual Review of

899   Marine Science*, *9*, 413–444. https://doi.org/10.1146/annurev-marine-010814-015924

900   Steinberg, D. K., Carlson, C. A., Bates, N. R., Goldthwait, S. A., Madin, L. P., & Michaels, A. F. (2000).

901   Zooplankton vertical migration and the active transport of dissolved organic and inorganic carbon

902   in the Sargasso Sea. *Deep Sea Research Part I: Oceanographic Research Papers*, *47*(1), 137–

903   158. https://doi.org/10.1016/S0967-0637(99)00052-7

904   Stramma, L., Johnson, G. C., Sprintall, J., & Mohrholz, V. (2008). Expanding Oxygen-Minimum Zones

905   in the Tropical Oceans. *Science*, *320*(5876), 655–658. https://doi.org/10.1126/science.1153847

906   Stukel, M. R., Décima, M., Landry, M. R., & Selph, K. E. (2018). Nitrogen and Isotope Flows Through

907   the Costa Rica Dome Upwelling Ecosystem: The Crucial Mesozooplankton Role in Export Flux.

908   *Global Biogeochemical Cycles*, *32*(12), 1815–1832. https://doi.org/10.1029/2018GB005968

909   Stukel, M. R., Ohman, M. D., Kelly, T. B., & Biard, T. (2019). The Roles of Suspension-Feeding and

910   Flux-Feeding Zooplankton as Gatekeepers of Particle Flux Into the Mesopelagic Ocean in the

911   Northeast Pacific. *Frontiers in Marine Science*, *6*. https://doi.org/10.3389/fmars.2019.00397

912   Tiano, L., Garcia-Robledo, E., Dalsgaard, T., Devol, A. H., Ward, B. B., Ulloa, O., et al. (2014). Oxygen

913   distribution and aerobic respiration in the north and south eastern tropical Pacific oxygen

914   minimum zones. *Deep Sea Research Part I: Oceanographic Research Papers*, *94*, 173–183.

915   https://doi.org/10.1016/j.dsr.2014.10.001

916 Turner, J. T. (2015). Zooplankton fecal pellets, marine snow, phytodetritus and the ocean's biological

917   pump. *Progress in Oceanography*, *130*, 205–248. https://doi.org/10.1016/j.pocean.2014.08.005

918 Van Mooy, B. A. S., Keil, R. G., & Devol, A. H. (2002). Impact of suboxia on sinking particulate organic

919   carbon: Enhanced carbon flux and preferential degradation of amino acids via denitrification.

920   *Geochimica et Cosmochimica Acta*, *66*(3), 457–465. https://doi.org/10.1016/S0016-

921   7037(01)00787-6

922 Weber, T., & Bianchi, D. (2020). Efficient Particle Transfer to Depth in Oxygen Minimum Zones of the

923   Pacific and Indian Oceans. *Frontiers in Earth Science*, *8*.

924   https://doi.org/10.3389/feart.2020.00376

925 Widner, B., Fuchsman, C. A., Chang, B. X., Rocap, G., & Mulholland, M. R. (2018). Utilization of urea

926   and cyanate in waters overlying and within the eastern tropical north Pacific oxygen deficient

927   zone. *FEMS Microbiology Ecology*, *94*(10). https://doi.org/10.1093/femsec/fiy138

928 Wilson, S. E., Steinberg, D. K., & Buesseler, K. O. (2008). Changes in fecal pellet characteristics with

929   depth as indicators of zooplankton repackaging of particles in the mesopelagic zone of the

930   subtropical and subarctic North Pacific Ocean. *Deep Sea Research Part II: Topical Studies in*

931   *Oceanography*, *55*(14–15), 1636–1647. https://doi.org/10.1016/j.dsr2.2008.04.019

932 Wishner, K. F., Outram, D. M., Seibel, B. A., Daly, K. L., & Williams, R. L. (2013). Zooplankton in the

933   eastern tropical north Pacific: Boundary effects of oxygen minimum zone expansion. *Deep Sea*

934   *Research Part I: Oceanographic Research Papers*, *79*, 122–140.

935   https://doi.org/10.1016/j.dsr.2013.05.012

936 Wishner, K. F., Seibel, B. A., Roman, C., Deutsch, C., Outram, D., Shaw, C. T., et al. (2018). Ocean

937   deoxygenation and zooplankton: Very small oxygen differences matter. *Science Advances*, *4*(12),

938   eaau5180. https://doi.org/10.1126/sciadv.aau5180

939   Wishner, K. F., Seibel, B., & Outram, D. (2020). Ocean deoxygenation and copepods: coping with

940   oxygen minimum zone variability. *Biogeosciences*, *17*(8), 2315–2339. https://doi.org/10.5194/bg-

941   17-2315-2020

942   Yang, C., Xu, D., Chen, Z., Wang, J., Xu, M., Yuan, Y., & Zhou, M. (2019). Diel vertical migration of

943   zooplankton and micronekton on the northern slope of the South China Sea observed by a moored

944   ADCP. *Deep Sea Research Part II: Topical Studies in Oceanography*, *167*, 93–104.

945   https://doi.org/10.1016/j.dsr2.2019.04.012

946

1 Supporting Information for

Slow particle remineralization, rather than suppressed disaggregation, drives efficient flux transfer through the Eastern Tropical North Pacific Oxygen Deficient Zone

2

3

4

5

6 Jacob A. Cram[1], Clara A. Fuchsman[1], Megan E. Duffy[2], Jessica L. Pretty[3], Rachel M.

7 Lekanoff[3], Jacquelyn A Neibauer[2], Shirley W. Leung[2], Klaus B. Huebert[1], Thomas S.

8 Weber[4], Daniele Bianchi[5], Natalya Evans[6], Allan H. Devol[2], Richard G. Keil[2], Andrew

9 M.P. McDonnell[3]

10

11 [1]Horn Point Laboratory, University of Maryland Center for Environmental Science,

12 Cambridge, MD, USA.

13 [2]School of Oceanography, University of Washington Seattle, Seattle, WA, USA.

14 [3]College of Fisheries and Ocean Sciences, University of Alaska Fairbanks, Fairbanks,

15 AK, USA.

16 [4]School of Arts and Sciences, University of Rochester, Rochester, NY, USA.

17 [5]Department of Atmospheric and Oceanic Sciences, University of California Los

18 Angeles, Los Angeles, CA, USA.

19 [6]Department of Biological Sciences, University of Southern California, Los Angeles, CA,

20 USA.

21

22 Contents of this file

23

24 Figures S1 to S12

25 Caption for Text S1

26

27 Additional Supporting Information (Files uploaded separately)

28

29 Text S1

1

30   Introduction

31   This file contains supplemental figures referenced in the manuscript. It also contains a

32   caption for a .PDF file containing mathematical equations underpinning the particle

33   remineralization model used.

2

34
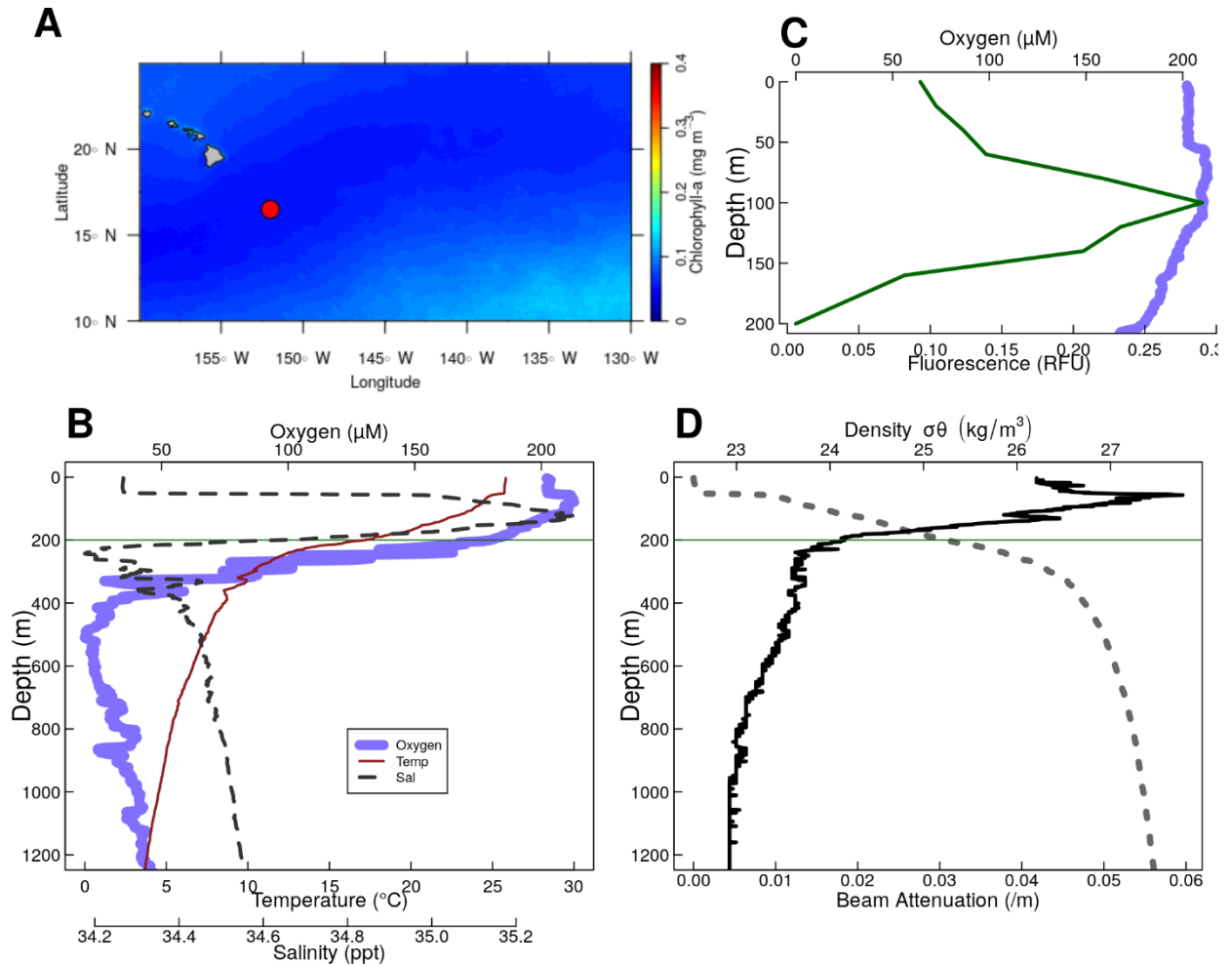
Figure S1. Physical and chemical data from P16 Station 100. Located at 16.5°N

152.0°W. (A) Map of the nearby tropical pacific station P16 Station 100. Colors indicate

chlorophyll concentrations at the surface, averaged over all MODIS images. The red

circle indicates the location of P16 Station 100. (B-D) Oceanographic parameters. The

thin horizontal green line shows the location of the base of the photic zone (200 m). (B)

Oxygen temperature and salinity. (C) Oxygen, and fluorescence. Because the fluorometer

was broken on this cruise, fluorescence data were pulled from world ocean atlas (Garcia

et al. 2014). (D) Beam attenuation and density, calculated from the salinity temperature

and pressure data.
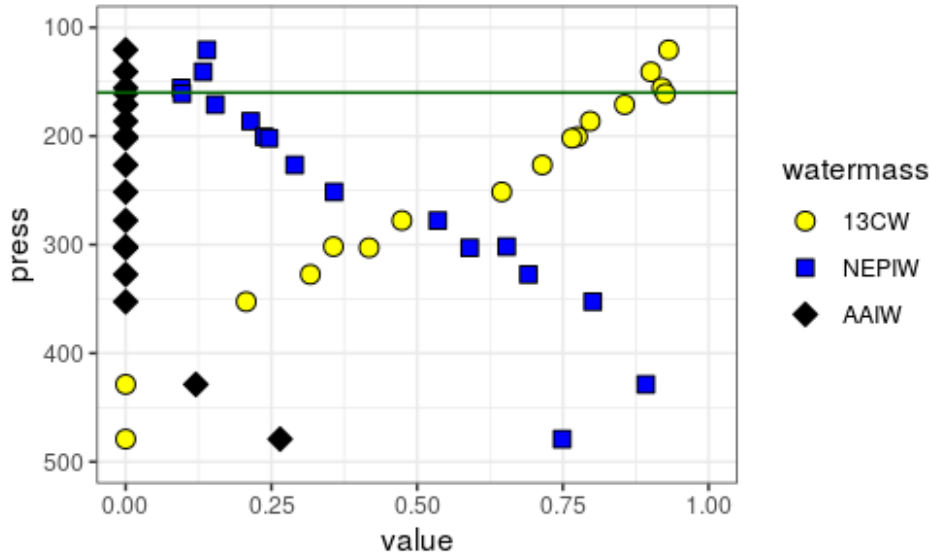
45

46 Figure S2. Water mass analysis at ETNP Station P2 indicates the relative contributions

47 proportions of the three primary water masses at this site, $13°C$ water (13CW), North

48 Equatorial Pacific Intermediate Water (NEPIW) and Antarctic Intermediate Water

49 (AAIW). Values indicate relative contributions of each water mass and are scaled so as to

50 sum to one. The horizontal green line indicates the base of the photic zone (160m). Data

51 are taken directly from Evans et al. (2020).

52
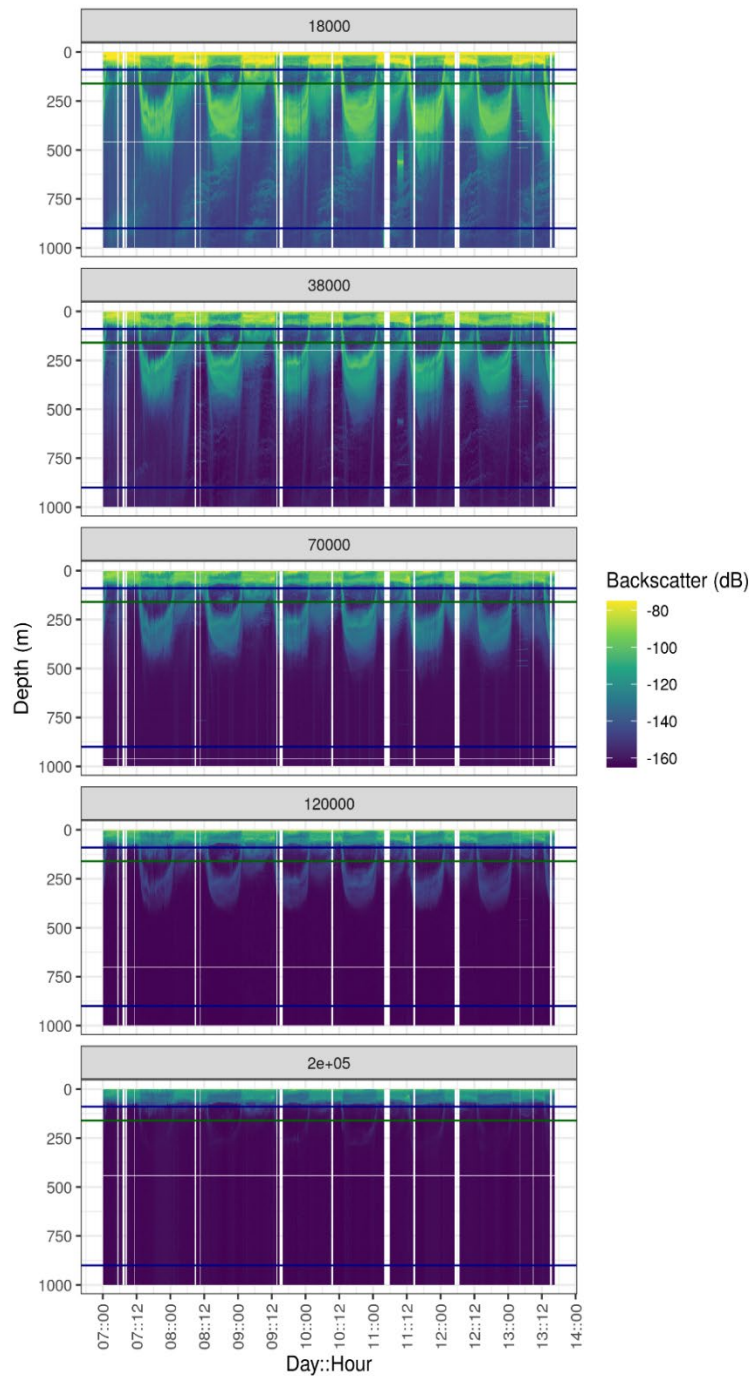
Figure S3. Acoustic data, measured by EK60, measured over the course of the

experiment, at ETNP Station P2. Shown are data from all frequency bands. Values are in

return signal intensity and have not been normalized to observed biomass. Horizontal

blue lines indicate the surface and bottom of the ODZ, while the horizontal green line

indicates the base of the photic zone.

5

58
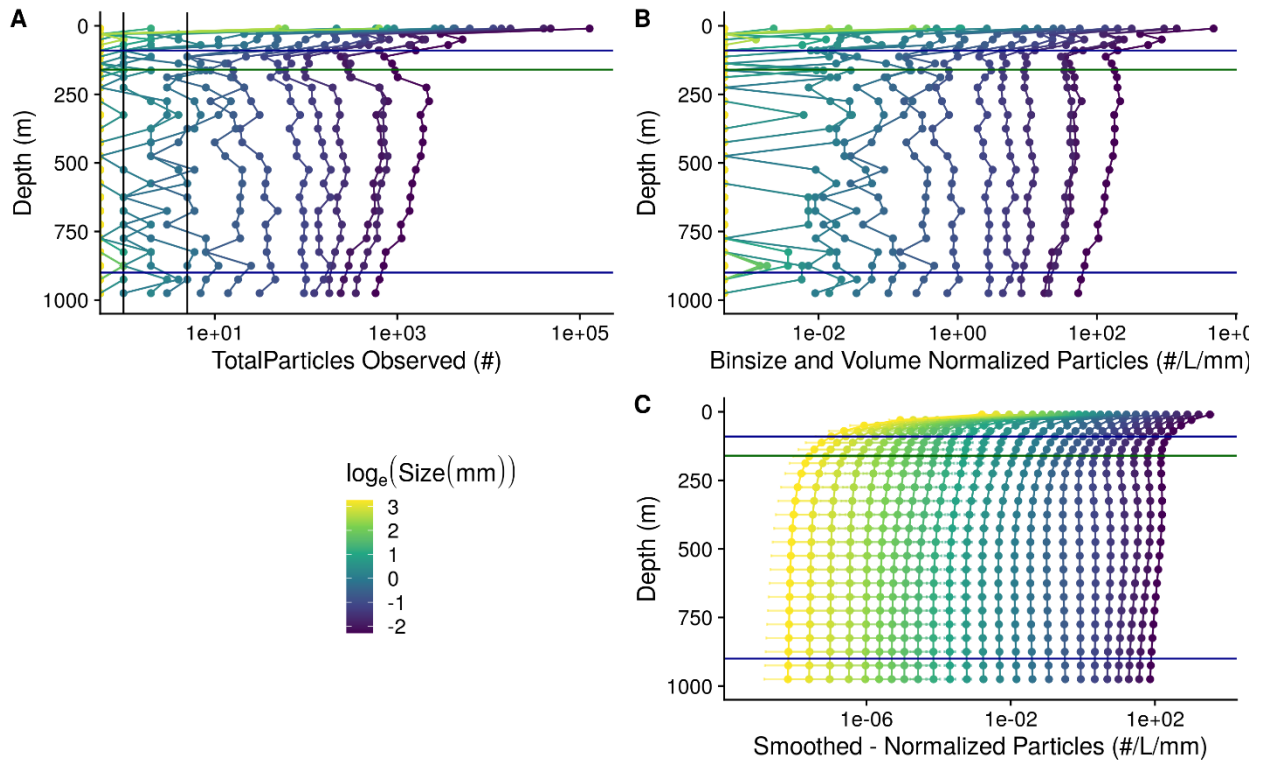
Figure S4. A profile of particle abundances at different sizes and depths, collected on
January 13 beginning at 06:13 at ETNP Station P2. Horizontal blue lines indicate the
surface and bottom of the ODZ, while the horizontal green line indicates the base of the
photic zone. (A) Numbers of observed particles. As the x axis is log transformed, zeros
are indicated as points along the Y axis. Vertical black lines indicate 1 and 5 observed
particles, respectively. (B) Particle numbers normalized to volume sampled and particle
size bin width. (C) Smoothed and extrapolated particle abundances, based on a negative
binomial GAM that predicts particle abundance form size and depth.

6
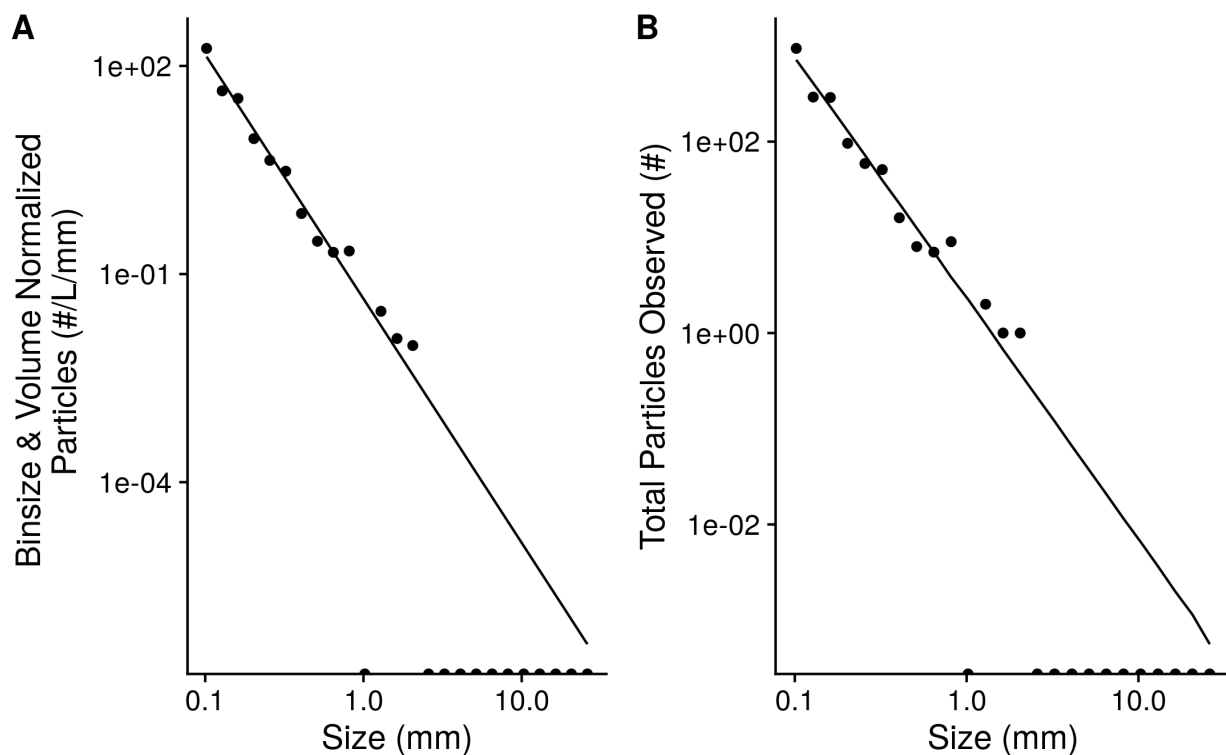
Figure S5. An example of observed particle size distribution spectra. These are depth binned data from between 150 and 175 m deep in the water column from the cast that occurred at *2017-01-13 17:51* local time at ETNP Station P2. This depth bin contains total numbers of particles that were seen across 206.8 L of merged UVP image volume. Points indicate (A) total numbers of observed particles and (B) particle numbers normalized to volume sampled and particle size bin width. Half-dots along the x axis correspond to particle size bins in which zero particles were observed. The line indicates the predicted best fit line of the data. The line was fit on the binsize and volume normalized data by a negative-binomial general linear model. The line in panel A indicates predictions from this same model, re-scaled into absolute particle space.

7
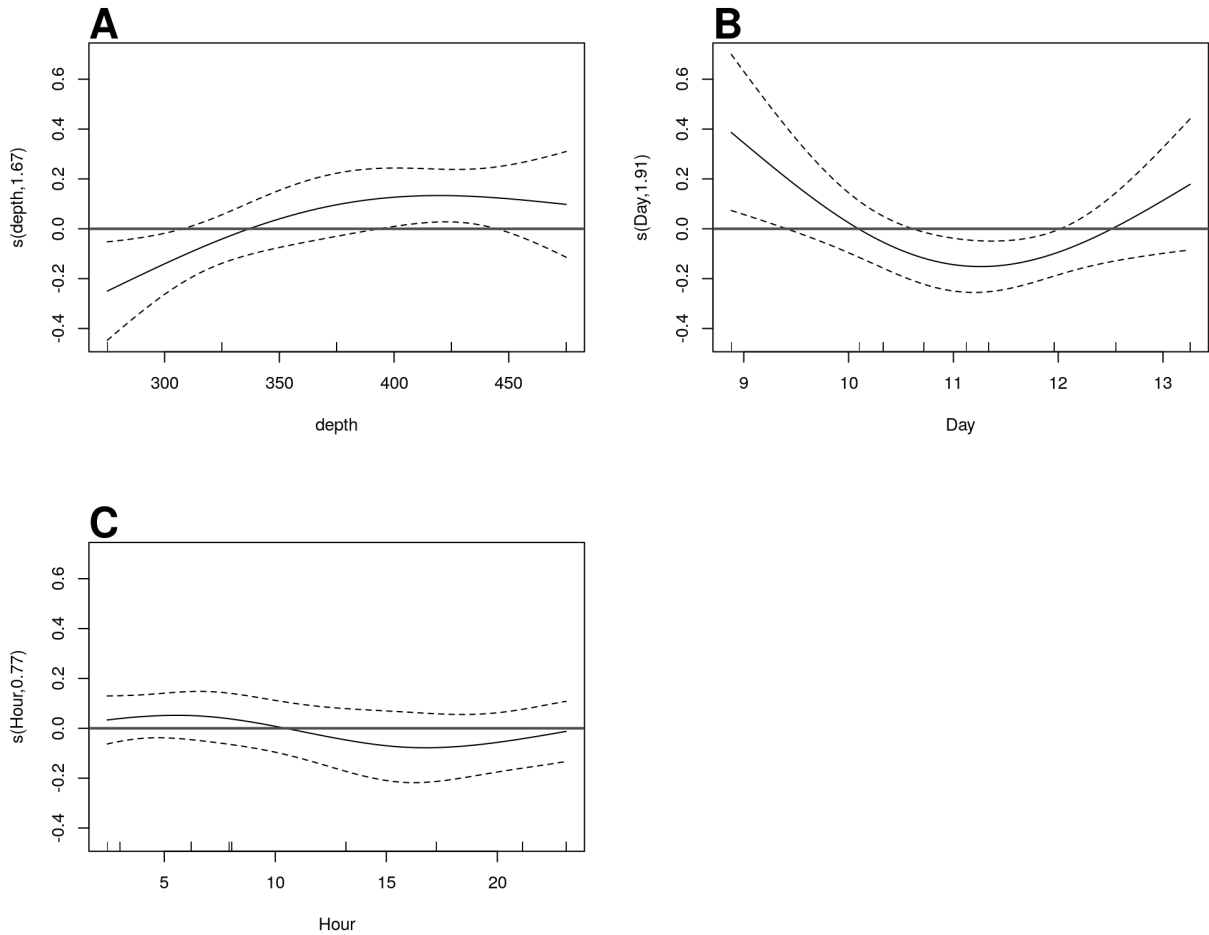
Figure S6. GAM predicted effects of A Depth, B Day of the month in January 2017, and
C hour of the day on the fifth-root transformed, depth normalized, rate of change of flux
at ETNP Station P2. Y axis indicates the value of the component smooth functions effect
on Flux. Positive values associate with times and regions of the water column where flux
is increasing, holding other factors constant, and negative ones where it is decreasing.
Horizontal gray line indicates $y = 0$, corresponding to that parameter having zero effect,
positive or on the outcome. Only Depth has a statistically significant relationship to rate
of change of flux (see section 6.5).
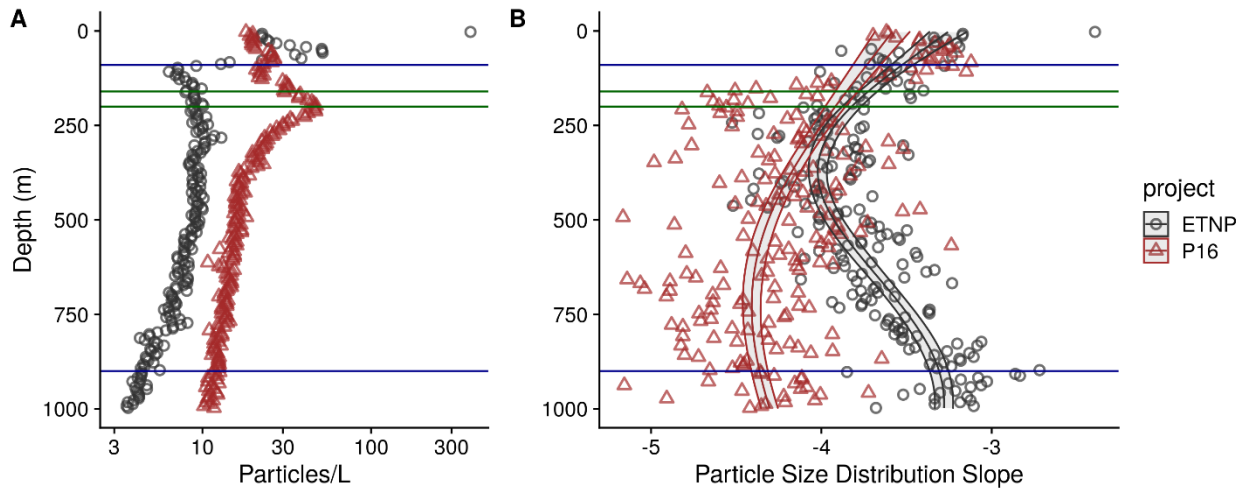
Figure S7. As above, but for the final cast taken at ETNP station P2 and the only cast collected from the P16 transect at Station 100. P16 Station 100 was chosen because it is at a similar latitude to ETNP station P2. (A) Total particle numbers, (B) Particle size distribution. Horizontal blue lines indicate the surface and bottom of the ODZ at the ETNP station, while the horizontal green lines indicate the bases of the photic zone at ETNP Station P2 (160m) and P16 Station 100 (200m).

9
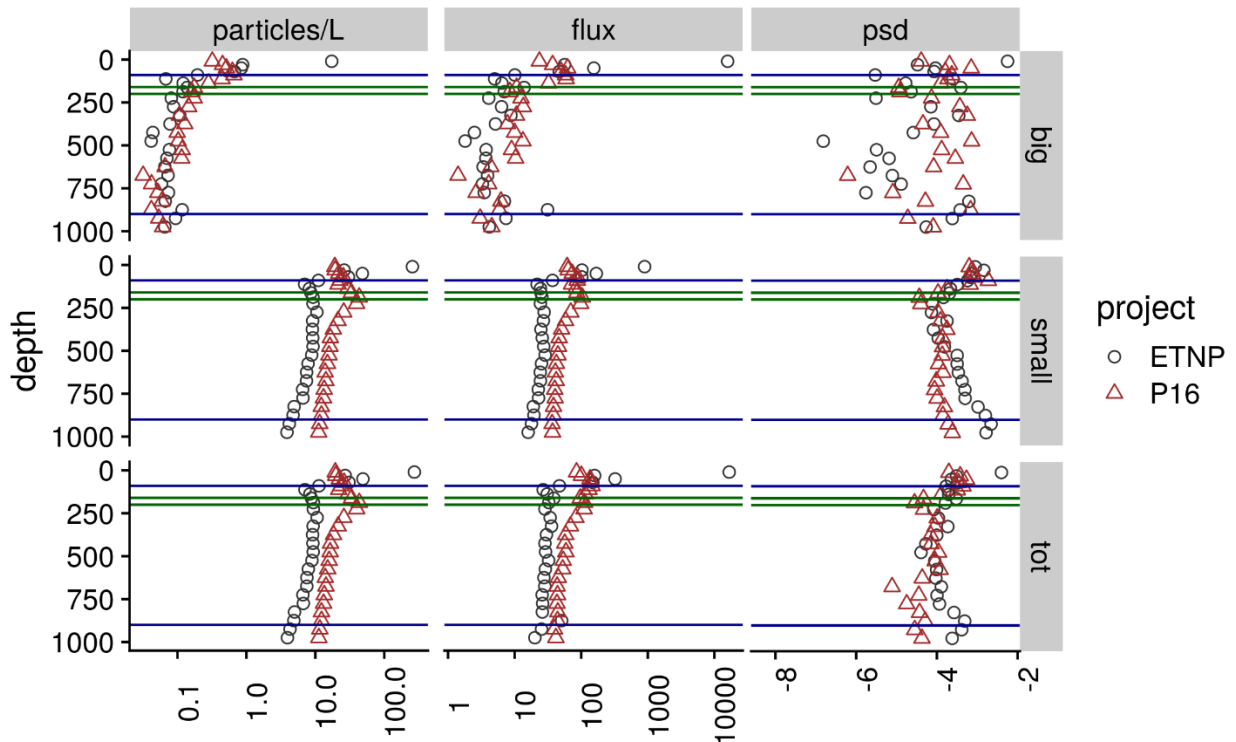
Figure S8. Depth binned particle number (volume normalized), particle size slope (PSD), and flux (estimated as in Fig. 4) for large ($>= 500\,\mu m$), small ($< 500\,\mu m$) and total particles, at the oxic (P16 Station 100) and anoxic site (ETNP Station P2). Within each panel, horizontal blue lines indicate the surface and bottom of the ODZ at the ETNP station, while the horizontal green lines indicate the bases of the photic zone at ETNP Station P2 (160m) and P16 Station 100 (200m).
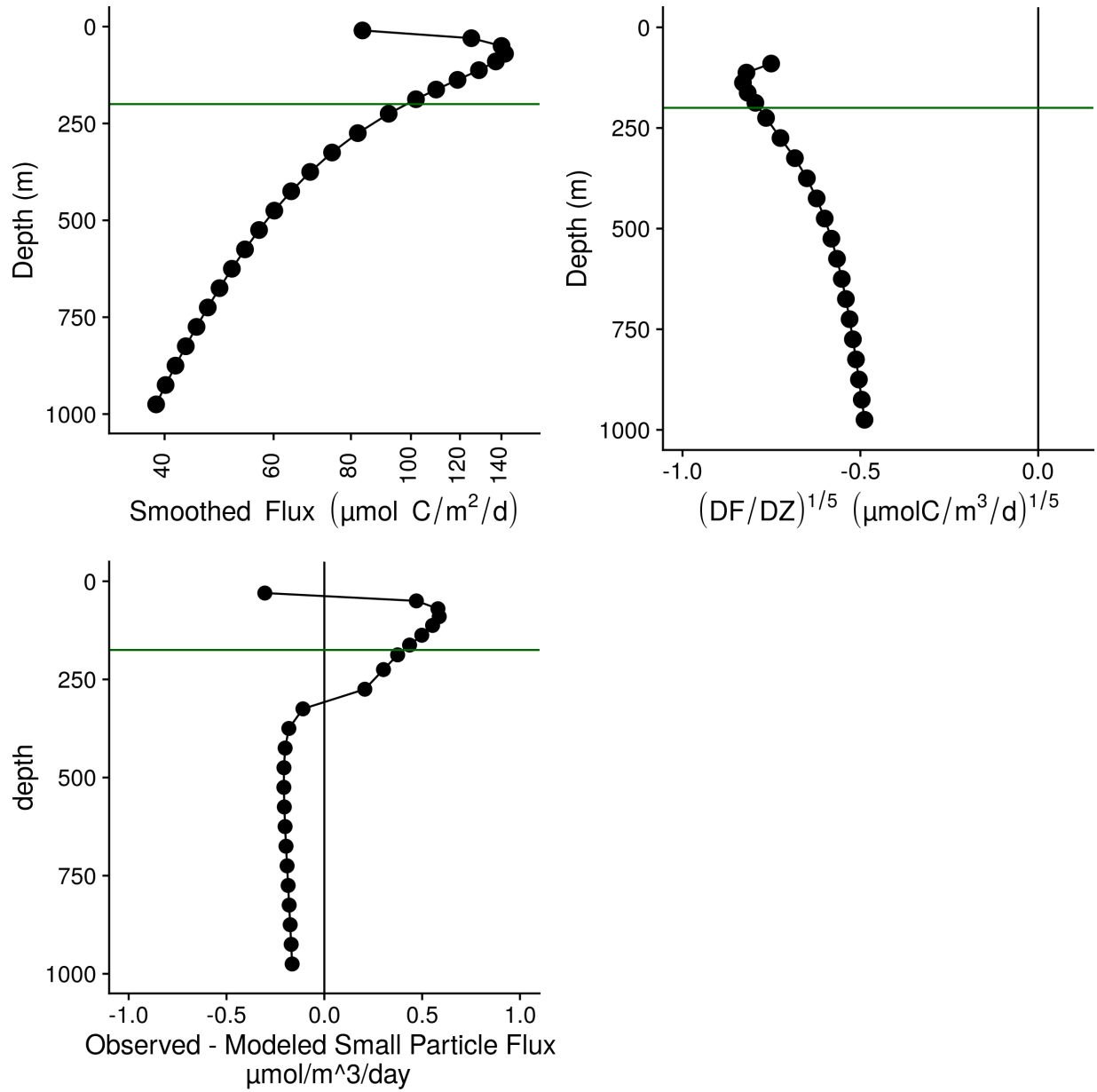
Figure S9. Flux profiles and flux attenuation at P16 Station 100. (A) Flux profile (B) Fifth-root transformed depth normalized rate of flux decrease. (C) Difference between observed and modeled results. Higher values suggest more disaggregation-like processes. The horizontal green line at 200 m indicates the base of the DCM as estimated by World Ocean Atlas data for this site.
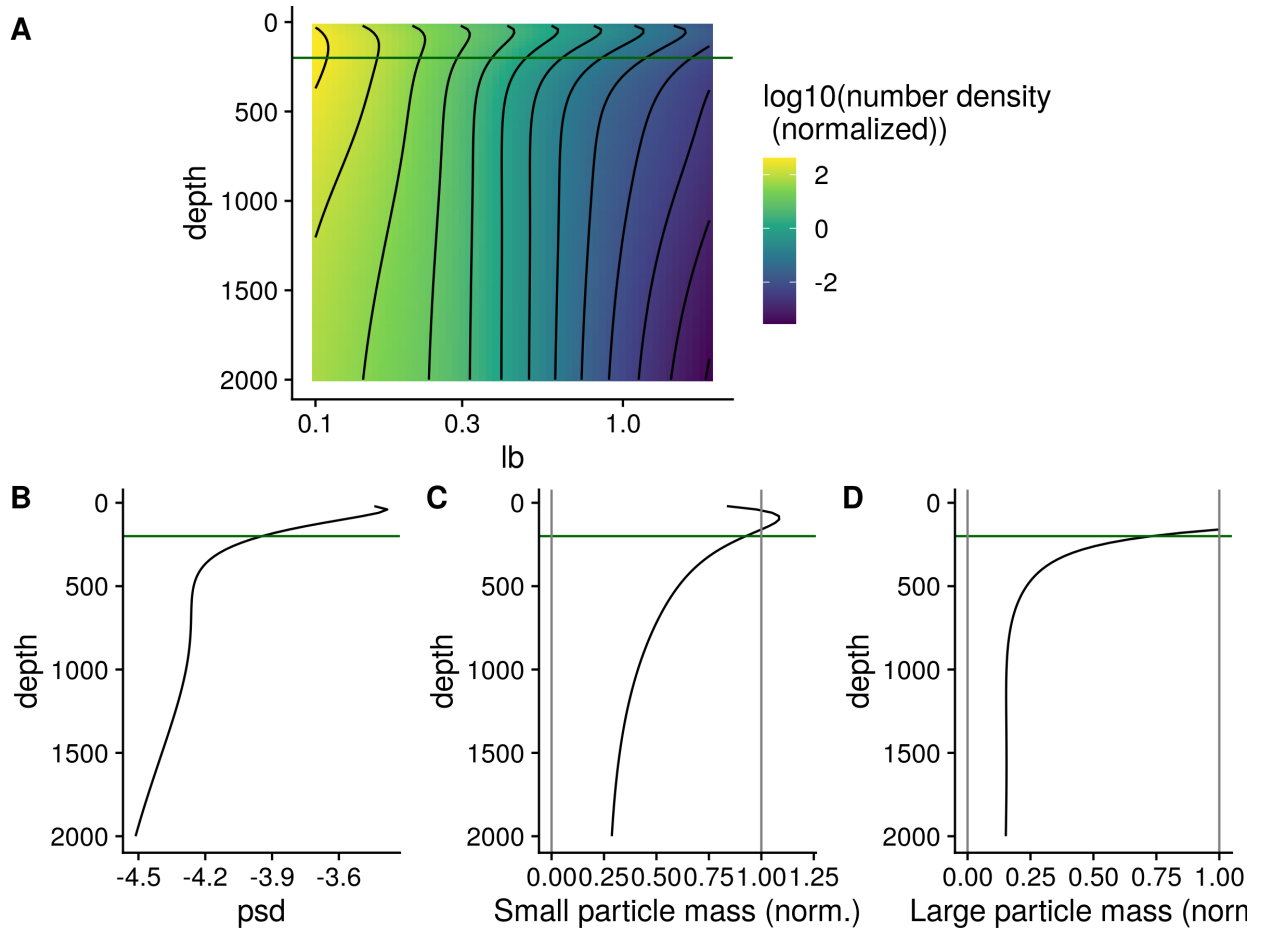
108
109　Figure S10. The same profiles as shown in Figure 5, but for the oxic site P16 Station

110　100. (A) GAM smoothed bin-size and volume particle numbers at each particle size class.

111　(B) Particle size distributions. And estimated biomass of (C) Small and (D) Large

112　particles. The horizontal green line at 200 m indicates the base of the DCM as estimated

113　by World Ocean Atlas data for this site.

114
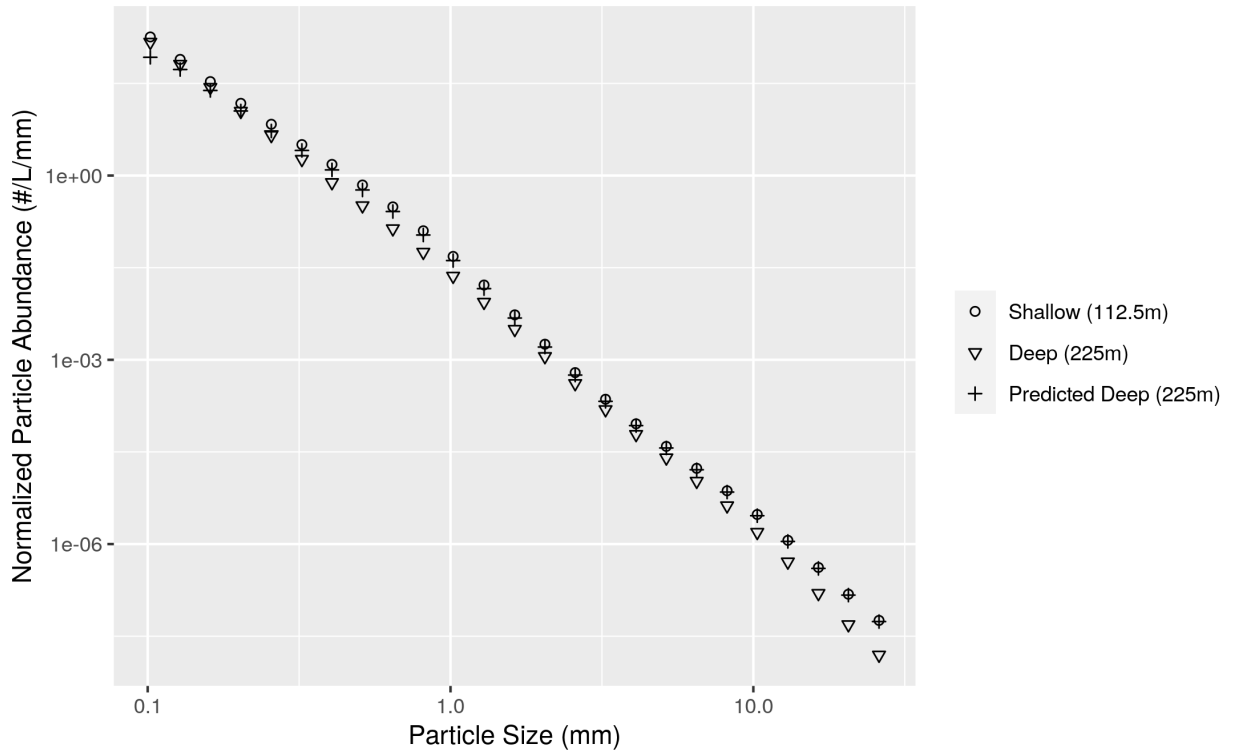
Figure S11. An example of differences between modeled and observed particle slope.
The particle size distribution at a shallow and a deeper depth, from ETNP Station P2, are
shown. The model generates a prediction of the deep depth profile from the shallow
depth profile and the flux attenuation between the two profiles. The model predicts more
attenuation of the smallest particles than is actually observed. In practice the model
compares depths that are closer together than the two shown here. In particular, the depth
bin above 225m in our analysis has a midpoint of 187.5m, but we choose in this example
to compare the 225m particle size profile to the profile at 112.5 m. Two depths that are
far apart are shown so that the flux attenuation is large enough to be seen by eye and to
provide a conceptual example of the models' function.

13
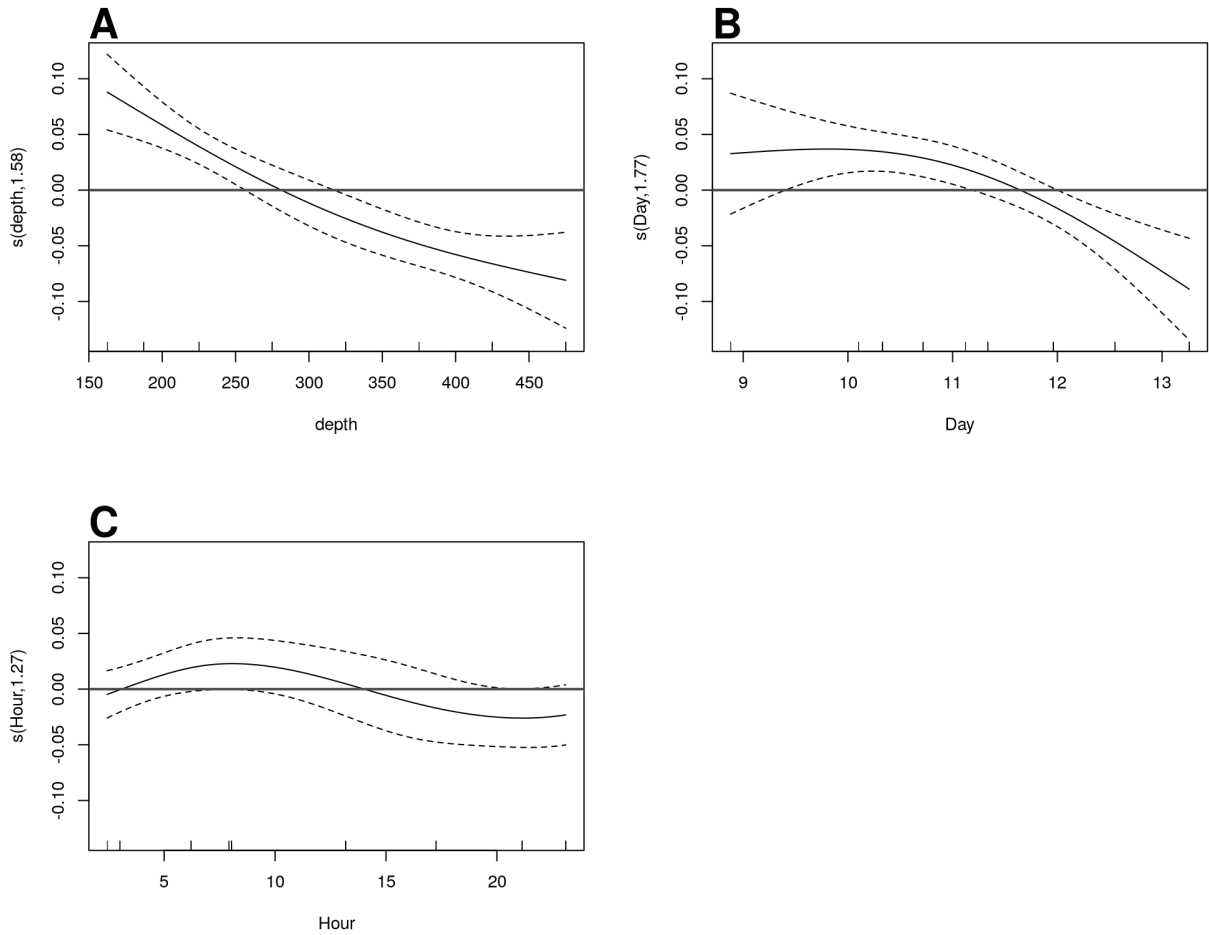
125

126   Figure S12. GAM predicted effects of A Depth, B Day of the month in January 2017, at

127   ETNP Station P2. Y axis indicates the value of the component smooth functions effect on

128   the difference between observed and modeled flux. Thus higher values correspond with

129   greater flux of small particles than predicted by the model. Horizontal gray line indicates

130   y = 0, corresponding to that parameter having zero effect, positive or on the outcome.

131   Only Depth and Day have a statistically significant relationship to rate of change of flux

132   (see Section 6.8).

133

134   Text S1. Full mathematical justification for the eularian version of the particle

135   remineralization and sinking model (PRiSM) model. Ful document uploaded separately.

14

Diagnosed Particle Disaggregation

Jacob A. Cram

May 21, 2021

1 Definitions and Units

$$m = C_m r^\alpha \tag{1}$$

As in DeVries et al. [2014] particle mass m is a function of radius r and scales with a fractal dimension α. C_m is a constant.

$$w = C_w r^\gamma \tag{2}$$

Sinking speed also scales with mass to another constant γ. According to Guidi et al. [2008] $\gamma = \alpha - 1$, but we'll keep things in terms of γ going forward.

$$F = nmw = nC_m C_w r^{\alpha+\gamma} \tag{3}$$

Flux F is a function of particle numbers, mass, and sinking speed.

Going forward we will determine the calculations for how many particles of size j in shallow depth i-1 remineralize into smaller particles of size j-1 in deeper depth i. We will call this term Δn_j

2 Conservation of particle number flux

In the absence of disaggregation, the number of particles leaving a box of water is equal to the number of particles going into that box from above. In other words, particle "number-flux" is conserved. Thus the number of particles in the box is a function of the number of particles going into that box, and the difference in velocities between when the particle enters and when that particle leaves.

$$n_{i-1,j-1}\frac{w_{j-1}}{w_j} + n_{i-1,j} = n_{i,j-1}\frac{w_{j-1}}{w_j} + n_{i,j} \tag{4}$$
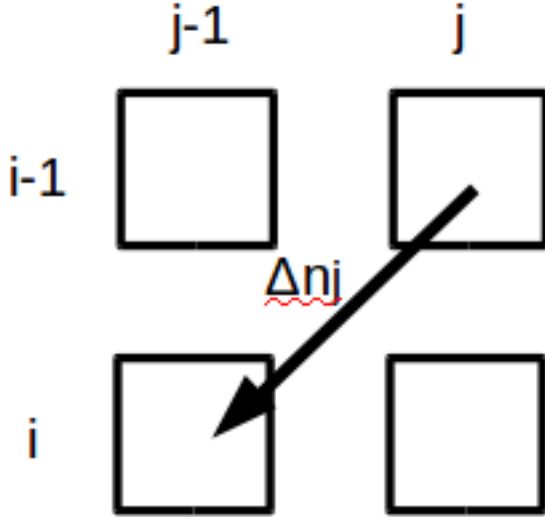
Figure 1: Some number of particles Δn_j of size "j" remineralize to size "j-1" as they sink from depth "i-1" to depth "i".

Where $n_{i-1,j}$ is the number of particles of size j (the bigger size) at depth i-1 (the shallower depth). The subscripts correspond to locations in Figure 1.

We can re-arrange equation 4

$$n_{i-1,j-1}w_{j-1} + n_{i-1,j}w_j = n_{i,j-1}w_{j-1} + n_{i,j}w_j \tag{5}$$

Substitue in equation 2 into equation 5.

$$n_{i-1,j-1}r_{j-1}^\gamma + n_{i-1,j}r_j^\gamma = n_{i,j-1}r_{j-1}^\gamma + n_{i,j}r_j^\gamma \tag{6}$$

Rearrange equation 6

$$r_{j-1}^\gamma(n_{i-1,j-1} - n_{i,j-1}) = r_j^\gamma(n_{i,j} - n_{i-1,j}) = \Phi \tag{7}$$

Where Φ is a placeholder standing for either side of equation 7, which I will subsequently substitute into things.

Solve for Δn_j

$$\Delta n_j = n_{i,j} - n_{i-1,j} = \frac{r_{j-1}^\gamma}{r_j^\gamma}(n_{i-1,j-1} - n_{i,j-1}) \tag{8}$$

3 Conservation of Mass Flux

Total flux defined is the sum of flux in each (observed) particle size bin. Particles not in an observed bin don't count towards total flux.

$$\Delta F = \sum_{j=2}^{n} \Delta f_j + \Delta f_1 \tag{9}$$

Here Δf_j is the flux attenuation from bin of size j and Δf_1 is the loss that comes from particles in bin 1 becoming small enough that you can no longer see them with the UVP.

The flux attenuation in a bin is the product of the rate of flux attenuation with depth of each individual particle $\frac{\partial f}{\partial z}$, the depth interval over which the particles attenuate Δz and the number of particles in that bin at the top of the depth interval $n_{i-1,j}$

$$\Delta f_j = \frac{\partial f}{\partial z} \Delta z n_{i-1,j} \tag{10}$$

Furthermore, the rate of flux attenuation with respect to depth is the product of the rate of mass attenuation with respect to time $\frac{\partial m}{\partial t}$, the inverse of the sinking speed $\frac{\partial t}{\partial z}$, and the deriviative of the flux to mass relationship $\frac{\partial f}{\partial m}$.

$$\frac{\partial f}{\partial z} = \frac{\partial m}{\partial z} \frac{\partial f}{\partial m} = \frac{\partial m}{\partial t} \frac{\partial t}{\partial z} \frac{\partial f}{\partial m} \tag{11}$$

In PRiSM, fractional mass loss as a function of time is the same for all particles of all sizes.

Now we are going to come up with the values for each of these terms.

The particle remineralization rate C_r is the same for particles of all sizes.

$$\frac{\partial m}{\partial t} = C_r * m = C_r C_m r^\alpha \tag{12}$$

Sinking speed definition, substituting from equation 2

$$\frac{\partial t}{\partial z} = \frac{1}{w} = \frac{1}{C_w r^\gamma} \tag{13}$$

Flux for a given size class, substituting eqation 1, and finally putting everything in terms of mass (rather than mass and radius, since the two are related)

$$f = mw = m * C_w r^\gamma = m * C_w (\frac{m}{C_m})^{\frac{\gamma}{\alpha}} \tag{14}$$

3

Derriving equation 14 with respect to mass, and substituting equation 1

$$\frac{\partial f}{\partial m} = Cw(1 + \frac{\gamma}{\alpha})(\frac{m}{Cm})^{\frac{\gamma}{\alpha}} = C_w(1 + \frac{\gamma}{\alpha})r^\gamma \tag{15}$$

Finally, we can construct our equation for flux attenuation by substituting equations 12, 13 and 15 into equation 11

$$\frac{\partial f}{\partial z} = C_r C_m r^\alpha (1 + \frac{\gamma}{\alpha}) \tag{16}$$

And now we can solve for equation 17.

$$\Delta f_j = C_r C_m r^\alpha (1 + \frac{\gamma}{\alpha}) \Delta z * n_{i-1,j} \tag{17}$$

We also need to solve for Δf_1 the flux "attenuation" that actually comes from particles leaving the smallest bin and escaping from what the UVP sees.

$$\Delta f_1 = \Delta n_1 m_1 w_1 = \Delta n_1 C_m C_w r_1^{\alpha+\gamma} \tag{18}$$

Here, Δn_1 is the number of particles leaving bin j = 1, but we haven't solved for that yet.

4 Solving for Δn_j

Recall that Δn_j is the number of particles that migrate between bin "j" and bin "j-1" as the particles sink from depth "i-1" to depth "i".

The flux at the shallower depth is equal to the flux at the deeper depth, plus the flux that attenuated between those two depths. Since $f = nmw$ and we know m and w

$$n_{i-1,j-1}C_m C_w r_{j-1}^{\alpha+\gamma} + n_{i-1,j}C_m C_w r_j^{\alpha+\gamma} = n_{i,j-1}C_m C_w r_{j-1}^{\alpha+\gamma} + n_{i,j}C_m C_w r_j^{\alpha+\gamma} + \Delta f_j \tag{19}$$

This equation can be re-arranged, and we can substitute in equation 17 for Δf_j.

The C_m cancel out.

$$C_w r_{j-1}^{\alpha+\gamma}(n_{i-1,j-1} - n_{i,j-1}) = C_w r_j^{\alpha+\gamma}(n_{i,j} - n_{i-1,j}) + C_r(1 + \frac{\gamma}{\alpha})\Delta z n_{i-1,j} r^\alpha \tag{20}$$

We can then substitute in Φ from equation 7.

$$C_w r_{j-1}^\alpha \Phi = C_w r_j^\alpha \Phi + C_r(1 + \frac{\gamma}{\alpha})\Delta z n_{i-1,j} r^\alpha \tag{21}$$

4

Rearrange

$$C_w\Phi(r_{j-1}^\alpha - r_j^\alpha) = Cr(1 + \frac{\gamma}{\alpha})\Delta z r^\alpha n_{i-1,j} \tag{22}$$

solve for Φ

$$\Phi = \frac{\frac{C_r}{C_w}\Delta z r^\alpha n_{i-1,j}(1 + \frac{\gamma}{\alpha})}{r_{j-1}^\alpha - r_j^\alpha} \tag{23}$$

$$\Delta n_j = \frac{\Phi}{r_j^\gamma} = \frac{\frac{C_r}{C_w}\Delta z r^\alpha n_{i-1,j}(1 + \frac{\gamma}{\alpha})}{r_j^\gamma(r_{j-1}^\alpha - r_j^\alpha)} \tag{24}$$

$$\Delta n_{j-1} = \frac{\Phi}{r_{j-1}^\gamma} = \frac{\Delta n_j r_j^\gamma}{r_{j-1}^\gamma} \tag{25}$$

At this point, the only unsolved variable is C_r, which we can now calculate.

5 Solving for C_r

We can calculate ΔF, the attenuation of flux and can impose the size spectrum and all of the other constants. Here we find the C_r that gives us the correct ΔF

First, to solve equation 9 by substituting in equaitons 17 and 18

$$\Delta F = \sum_{j=2}^n \Delta f_j + \Delta f_1 = \sum_{j=2}^n \left\{ C_r C_m r_j^\alpha(1 + \frac{\gamma}{\alpha})\Delta z n_{i-1,j} \right\} + \Delta n_1 C_m C_w r_1^{\alpha+\gamma} \tag{26}$$

Substitute equation 24 for Δn_j when j = 1 for Δn_1

$$\Delta F = \sum_{j=2}^n \Delta f_j + \Delta f_1 = \sum_{j=2}^n \left\{ C_r C_m r_j^\alpha(1 + \frac{\gamma}{\alpha})\Delta z n_{i-1,j} \right\} + \frac{\frac{C_r}{C_w}\Delta z r_1^\alpha n_{i-1,1}(1 + \frac{\gamma}{\alpha})}{r_1^\gamma(r_0^\alpha - r_1^\alpha)} C_m C_w r_1^{\alpha+\gamma} \tag{27}$$

In the above, r_0 is the effective size of the particles smaller than the UVP can see. In principle this is arbitrary. Numbers closer to zero result in fewer particles in the smallest bin disapearing, larger ones to more of those particles disapearing. As r_0 approaches r_1 Cr approaches zero. They cannot be equal or the math breaks.

Pull what I can out of the sum operation, and cancel out r^γ and C_w from the rightmost term

$$\Delta F = C_r C_m \Delta z (1 + \frac{\gamma}{\alpha}) \sum_{j=2}^{n} \left\{ r_j^\alpha n_{i-1,j} \right\} + \frac{C_r \Delta z r_1^{2\alpha} n_{i-1,1}(1 + \frac{\gamma}{\alpha})}{(r_0^\alpha - r_1^\alpha)} C_m \qquad (28)$$

Now we can solve for C_r

$$C_r = \frac{\Delta F}{C_m \Delta z (1 + \frac{\gamma}{\alpha}) \left[\sum_{j=2}^{n} \left\{ r_j^\alpha n_{i-1,j} \right\} + \frac{r_1^{2\alpha} n_{i-1,1}}{r_0^\alpha - r_1^\alpha} \right]} \qquad (29)$$

Thus for a pair of profiles, we can estemate the flux attenuation, calculate Cr from that, and then plug Cr (and the profile) into the equation 24 for Δn_j. We can thus compute Δn_j for each size class to see how many particles from that bin move to the next bin smaller.